# Landslide tsunamis: Comparison between depth-averaged and Navier–Stokes models

Alexandre Paris, Philippe Heinrich, Stéphane Abadie

# Landslide tsunamis: Comparison between depth-averaged and Navier-Stokes models

Alexandre Paris[1,2], Philippe Heinrich[1], and Stéphane Abadie[2]

[1]CEA, DAM, DIF, 91297 Arpajon Cedex, France

[2]Université de Pau et des Pays de l'Adour, E2S UPPA, SIAME, Anglet, France

**Abstract**

Two approaches are proposed to simulate tsunamis generated by granular landslides: a depth-averaged model, AVALANCHE, and laminar Navier-Stokes simulations using the OpenFOAM model. Both models are validated against two 2D benchmarks, a subaerial and a submerged one involving a triangle initial slide shape. In both models, the landslide is defined as a viscous fluid flowing downslope. Except in the first instants, both models can reproduce either the landslide behavior or the generated first water waves but can not reproduce simultaneously both the landslide and the water surface. There is an overlap in the optimal viscosity range between both models. Sensitivity studies are carried out by varying the slope angle and the landslide submergence for the subaerial benchmark. The largest waves are obtained for initial landslide position close to the free surface. The height of the generated waves increases linearly with the slope angle and the landslide Reynolds number in the depth-averaged model. The relationships are more complex in the Navier-Stokes model. For low slide Reynolds numbers and with an initial slide close to the free surface, both models produce similar waves. Nine additional cases are performed with a $k-\epsilon$ turbulence closure model and varying the submergence and the slope angle.

## 1 Introduction

Landslide tsunamis have been reported in coastal areas such as fjords (Naranjo et al. 2009, L'Heureux et al. 2012), rivers (Lefebvre et al. 1991) and volcanic islands (Tinti et al. 1999, Heinrich et al. 2001b, Tinti et al. 2006), in deep water (Bondevik et al. 2005) or in closed water basins such as lakes (Wang et al. 2015, Gylfadóttir et al. 2017) and reservoirs (Ward & Day 2011, Xiao et al. 2015). They constitute a major natural hazard for coastal populations and infrastructure and therefore a better understanding of the processes involved is required.

Since the early 2000s, the interest for landslide tsunamis has grown considerably. An extensive literature is available on historical cases and their diverse numerical simulations (L'Heureux et al. 2011, Ward & Day

2011, Redfield et al. 2011, Franz et al. 2015, Wang et al. 2015, Xiao et al. 2015, Glimsdal et al. 2016, Huang et al. 2017, Gylfadóttir et al. 2017, Haeussler et al. 2018, Grilli et al. 2019). Landslide tsunamis are rarely observed therefore their study is generally based on experimental or numerical models. Recent reviews of landslide tsunamis models can be found in Yavari-Ramshe & Ataie-Ashtiani (2016) and Kim et al. (2020). The studies associated to the last significant reported event, the December 23, 2018 Anak Krakatau collapse, which generated a 80 to 100 m high tsunami in the near-field and 1 to 2 m water waves on the coasts of the Sunda Strait (Grilli et al. 2019, Paris et al. 2020, Heidarzadeh et al. 2020, Borrero et al. 2020), illustrate the plurality of the numerical models usually employed. Grilli et al. (2019) used a 3D model (NHWAVE) for the landslide tsunami generation and a 2D depth-integrated (2DH) model (FUNWAVE-TVD) for the tsunami propagation; Paris et al. (2020), a unique 2DH model (AVALANCHE) for the landslide simulation, the tsunami generation and propagation; Heidarzadeh et al. (2020), a 2DH model (COMCOT) for the tsunami propagation with a simple initial elevation in order to introduce a generated water wave and Borrero et al. (2020) a 2DH model (pCOULWAVE) with an initial tsunami waveform derived from an analytical solution. This highlights the existence of two methods to simulate landslide tsunamis. In the first one, the landslide is simulated separately and then introduced in a tsunami propagation model as an initial perturbation. In the second, landslide simulation, tsunami generation and propagation take place in the same model. The first approach allows to simulate the landslide with a more realistic 3D model before using a faster 2DH model for the tsunami propagation (Grilli et al. 2019, Abadie et al. 2020). The second approach has the advantage of being more flexible since only one code is needed. Moreover, the computational cost may be lower when both landslide and tsunami simulations are based on depth-averaged equations.

The landslide rheology is also a critical parameter in a landslide tsunami model. Numerical models considering rigid landslide (Fuhrman & Madsen 2009, Ataie-Ashtiani & Yavari-Ramshe 2011, Bosa & Petti 2011, Dutykh & Kalisch 2013) are opposed to deformable landslides models (Serrano-Pacheco et al. 2009, Kelfoun et al. 2010, Glimsdal et al. 2016, Huang et al. 2017). Among the last category, the landslide can be defined, for example, as a granular flow following a Coulomb law friction (Mangeney et al. 2000, Kelfoun et al. 2010, Macías et al. 2015), or as a viscous fluid, considering a Newtonian fluid (Abadie et al. 2012, Horrillo et al. 2013) or non-Newtonian Bingham fluid (Skvortsov & Bornhold 2007, Serrano-Pacheco et al. 2009). Note that the last recent works introduced a two-phase formulation for a granular landslide combined with a volume of fluid model to capture the air-water interface (Si et al. 2018, Lee & Huang 2021).

Comparison between 2DH and 3D models have been carried out for seismic tsunamis propagation (Sogut & Yalçiner 2019), tsunami inundation (Qin et al. 2018a, Horrillo et al. 2015, Sogut & Yalçiner 2019) and generated coastal currents (Lynett et al. 2017, Sogut & Yalçiner 2019). In Kim et al. (2020), the authors question the applicability of 2DH models to landslide tsunamis, suggesting that 3D models taking into account the vertical acceleration would produce more accurate results. Over the past two decades, several 3D models based on Navier-Stokes equations have been developed, among them, THETIS (Abadie et al.

2008), FLUENT (Biscarini 2010), Fluidity (Davies et al. 2011), NHWAVE (Ma et al. 2013), TSUNAMI3D (Horrillo et al. 2013), Splash3D (Wu et al. 2020) and OpenFOAM (Lee et al. 2016, Si et al. 2018, Romano et al. 2020, Lee & Huang 2021). However, an extensive comparison between 2D and 3D models for landslide tsunamis generation is, to the knowledge of the authors of this present study, not available.

Models validation often relies on analytical solutions, laboratory experiments or real cases. The literature reports experiments using rigid landslides, made of aluminium (Liu et al. 2005, Enet & Grilli 2007, Sue et al. 2011), rock (Bolin et al. 2014) or PVC (Heller & Spinneken 2015), deformable landslides made of rocks/gravel (Mazzanti & Vittorio de Blasio 2011, Mohammed & Fritz 2012, Bregoli et al. 2013, McFall & Fritz 2016), $BaSO_4$/polypropylene grains (Evers et al. 2019), ceramics beads (Mulligan & Take 2017), glass beads (Viroulet et al. 2016, Grilli et al. 2017) or simply water (Bullard et al. 2019). Experiments are either submerged or subaerial, on slopes generally ranging from 15° (Enet & Grilli 2007, Sue et al. 2011) to 45° (Heller & Spinneken 2015, Viroulet et al. 2016) or more (up to 70° for Bolin et al. (2014) and 90° for Evers et al. (2019)). The main objective of the present study is to identify the application fields of depth-averaged models (represented here by AVALANCHE) by comparing the results of simulations over a large range of parameters with a Navier-Stokes model (here OpenFOAM, in laminar mode). To achieve this objective, both models are tested against two laboratory experiments: one subaerial (Viroulet et al. 2016) and one submerged (Grilli et al. 2017). For these two benchmarks, the comparison between experiments and simulations is made for both the landslide behavior and the generated water waves. Then, the initial configuration of one of the experiment considered for benchmark is modified and simulations are realized by varying the slope angle and the depth of submergence of the slide. Finally, nine of the previous simulations are run in turbulent mode considering a $k - \epsilon$ model.

In Section 2, we present the AVALANCHE and the OpenFOAM models. Section 3 is devoted to the description of the benchmarks, the numerical simulations and the sensitivity studies. Results are presented in Section 4 and a discussion is given in Section 5.

# 2 Models presentation

## 2.1 Depth-averaged model: AVALANCHE

AVALANCHE is a 2DH code designed to simulate the landslide and the generated tsunami. It is written in Fortran 90/95 and parallelized via the MPI library. The landslide can be modeled either as a granular flow, falling under gravity and following a Coulomb friction law, or as a viscous Newtonian fluid. The code can use a system of nested grids with a coarse grid over deep water regions and fine grids over coastal regions to model local effects of bathymetry. It has been successfully employed to simulate both subaerial (Heinrich & Piatanesi 2000, Hébert et al. 2002, Le Friant et al. 2003, Paris et al. 2019, 2020) and submarine landslides (Rodriguez et al. 2013, Poupardin et al. 2017).

The landslide part is governed by the following equations set adapted from the one-phase grain-flow model of Savage & Hutter (1989) using here a viscous fluid (to be consistent with the rheological law of the Navier-Stokes model) and written in a coordinates system ($x'$,$y'$) parallel to the slope:

$$\frac{\partial h_s}{\partial t} + \frac{\partial}{\partial x'}(h_s u_s) + \frac{\partial}{\partial y'}(h_s v_s) = 0 \tag{1}$$

$$\frac{\partial}{\partial t}(h_s u_s) + \frac{\partial}{\partial x'}(h_s u_s^2) + \frac{\partial}{\partial y'}(h_s u_s v_s) = -\frac{1}{2}\kappa\frac{\partial}{\partial x'}(g h_s^2 \cos\theta) + \kappa g h_s \sin\theta_x + \tau_{x'z'(z'=0)} \tag{2}$$

$$\frac{\partial}{\partial t}(h_s v_s) + \frac{\partial}{\partial x'}(h_s v_s u_s) + \frac{\partial}{\partial y'}(h_s v_s^2) = -\frac{1}{2}\kappa\frac{\partial}{\partial y'}(g h_s^2 \cos\theta) + \kappa g h_s \sin\theta_y + \tau_{y'z'(z'=0)'} \tag{3}$$

where $h_s$ is the slide's thickness in a direction perpendicular to the slope, $\mathbf{u} = (u_s, v_s)$ the depth-averaged velocity vector parallel to the bed, $\kappa = 1 - \rho_w/\rho_s$ where $\rho_w$ and $\rho_s$ are the water and rock densities (for the subaerial part of the slide, $\kappa$ is identically equal to 1), $\theta(x, y)$ the local steepest slope angle, $\theta_x$ and $\theta_y$ the slope angles along the $x$ and $y$ axes respectively, and $\tau_z = -\nu\rho_w\mathbf{u}/(h_s\rho_s)$ the shear stress at the bed surface for a uniform profile of the horizontal velocity, where $\nu$ is the kinematic viscosity.

The tsunami propagation can be simulated by solving either the shallow water equations (4), (5), (6) or the Boussinesq equations of Løvholt et al. (2008) (7), (8), (9). A switch between the two sets of equations allows to use the shallow water equations for a few instants during the water wave generation in the near-field and the Boussinesq model for the far-field propagation. Indeed, Audusse et al. (2021) showed that this combination of models improves the simulation of the generation process compared to using only the Boussinesq model.

*Shallow water equations*

$$\frac{\partial \eta}{\partial t} + \frac{\partial (hu)}{\partial x} + \frac{\partial (hv)}{\partial y} = -\frac{\partial d_w}{\partial t} \tag{4}$$

$$\frac{\partial u}{\partial t} + u\frac{\partial u}{\partial x} + v\frac{\partial u}{\partial y} = -g\frac{\partial \eta}{\partial x} + F_x \tag{5}$$

$$\frac{\partial v}{\partial t} + u\frac{\partial v}{\partial x} + v\frac{\partial v}{\partial y} = -g\frac{\partial \eta}{\partial y} + F_y \tag{6}$$

where $\eta$ is the surface elevation, $h$=$\eta$+$d$ the water column height with $d$ the initial depth, $d_w$ the sea-bottom deformation due to the landslide, $u$ and $v$ the depth-averaged velocities along the $x$ and $y$ axes respectively and $F_x$ and $F_y$ the friction and Coriolis forces, which are assumed to be negligible in our modeling.

*Boussinesq equations*

$$\frac{\partial \eta}{\partial t} + \frac{\partial (hu)}{\partial x} + \frac{\partial (hv)}{\partial y} = -\frac{\partial d_w}{\partial t} \tag{7}$$

$$\frac{\partial u}{\partial t} + u\frac{\partial u}{\partial x} + v\frac{\partial u}{\partial y} = -g\frac{\partial \eta}{\partial x} + \frac{d^3}{3}\left[\frac{\partial^2 u_t}{\partial x^2} + \frac{\partial^2 v_t}{\partial x \partial y}\right] + \frac{d}{2}\left[u_t\frac{\partial^2 d}{\partial x^2} + u_t\frac{\partial^2 d}{\partial x \partial y}\right] + d\frac{\partial d}{\partial x}\frac{\partial u_t}{\partial x} + \frac{d}{2}\left[\frac{\partial d}{\partial x}\frac{\partial v_t}{\partial y} + \frac{\partial d}{\partial y}\frac{\partial v_t}{\partial x}\right] + F_x \quad (8)$$

$$\frac{\partial v}{\partial t} + u\frac{\partial v}{\partial x} + v\frac{\partial v}{\partial y} = -g\frac{\partial \eta}{\partial y} + \frac{d^3}{3}\left[\frac{\partial^2 v_t}{\partial y^2} + \frac{\partial^2 u_t}{\partial x \partial y}\right] + \frac{d}{2}\left[v_t\frac{\partial^2 d}{\partial y^2} + v_t\frac{\partial^2 d}{\partial x \partial y}\right] + d\frac{\partial d}{\partial y}\frac{\partial v_t}{\partial y} + \frac{d}{2}\left[\frac{\partial d}{\partial x}\frac{\partial u_t}{\partial y} + \frac{\partial d}{\partial y}\frac{\partial u_t}{\partial x}\right] + F_y \quad (9)$$

where $u_t$ and $v_t$ the time-derivatives of $u$ and $v$.

The sea-bottom deformation due to the landslide is transmitted to the water surface by applying a filter in order to spread out the water deformation at the surface following Kelfoun et al. (2010):

$$\Delta d_w = a \times \frac{V}{b^2} \times e^{-\ln(\pi)\times\frac{b}{h}} \quad (10)$$

where $V$ is the volume displaced vertically at the bottom, $a$ is a parameter that allows mass conservation in order that $\int_{x=-\infty}^{\infty}\int_{y=-\infty}^{\infty}\Delta d_w dxdy = V$, and $b = \sqrt{x^2+y^2+h^2}$ is the distance between a given point $(x, y, h)$ of the water surface and the point at the bottom $(x = 0, y = 0, z = 0)$ where volume change occurs. This formula of the sudden elevation of the water is exact for a horizontal plane at the bottom and is assumed to be a good approximation in steep slopes environments.

## 2.2 Navier-Stokes model: OpenFOAM

OpenFOAM (Open-source Field Operation And Manipulation) is an open source CFD software developed by OpenCFD Ltd since 2004. It allows to simulate multiphase flow, solving the 3D Navier-Stokes equations. It is written in C++ and uses a system of modules that the user can assemble to build his own case and in which all the files can be modified. OpenFOAM is able to deal with incompressible/compressible turbulence, thermophysical, multiphase or wave modeling. It handles the mesh generation, the case simulation and the reading and postprocessing of the outputs.

Among others, it was used by Qin et al. (2018b) to study the inundation and impact of a tsunami on a coastal city or by Honarmand et al. (2020) to propagate the initial elevation generated by the Makran earthquake in 1945. Romano et al. (2020) also developed an approach to simulate tsunamis generated by a solid landslide using the Overset mesh technique. Considering a deformable landslide, Rauter et al. (2021) reproduced the experiments of Bullard et al. (2019) using the solver multiphaseInterFoam with two viscous fluids. Closer to the present work since it concerns the same benchmarks, Si et al. (2018), Yu & Lee (2019)

and Lee & Huang (2021) used models based on OpenFOAM to simulate the subaerial experiments of Viroulet et al. (2016) and submerged experiments of Grilli et al. (2017), respectively. The first authors introduced a granular temperature in the granular phase, while the second ones used a Navier-slip boundary condition adapted for granular flows.

As Rauter et al. (2021), we use the Navier-Stokes equations to simulate three fluids (air, water and sediment). The continuity equation reads:

$$\nabla \cdot \mathbf{u} = 0 \tag{11}$$

where $\mathbf{u}$ is the velocity, and the momentum equation reads:

$$\frac{\partial \rho \mathbf{u}}{\partial t} + \nabla \cdot (\rho \mathbf{u}\mathbf{u}) = -\nabla p + \nabla \cdot (2(\mu + \mu_t)\mathbf{D}) + \rho \mathbf{g} \tag{12}$$

where $\mathbf{D}$ is the strain rate tensor, $\mathbf{g}$ the gravitational acceleration, $p(\mathbf{x}, t)$ the pressure field, and $\rho$, $\mu$ and $\mu_t$ are the local fluid density, molecular dynamic viscosity and eddy viscosity, respectively and are defined as follows:

$$\rho = \sum_i \alpha_i(\mathbf{x}, t)\rho_i \tag{13}$$

$$\mu = \sum_i \alpha_i(\mathbf{x}, t)\mu_i \tag{14}$$

$$\mu_t = \rho C_\mu \frac{k^2}{\epsilon} \tag{15}$$

where $\epsilon$ is the turbulent kinetic energy dissipation rate and k is the turbulent kinetic energy. They are implemented as follows:

$$\frac{\partial}{\partial t}(\alpha\rho\epsilon) + \nabla \cdot (\alpha\rho\mathbf{u}\epsilon) - \nabla^2(\alpha\rho D_\epsilon \epsilon) = C_1 \alpha\rho G \frac{\epsilon}{k} - \left(\left(\frac{2}{3}C_1 - C_{3,RDT}\right)\alpha\rho\nabla \cdot \mathbf{u}\epsilon\right) - \left(C_2 \alpha\rho \frac{\epsilon}{k}\epsilon\right) + S_\epsilon + S_{fvOptions} \tag{16}$$

$$\frac{\partial}{\partial t}(\alpha\rho k) + \nabla \cdot (\alpha\rho\mathbf{u}k) - \nabla^2(\alpha\rho D_k k) = \alpha\rho G - \left(\frac{2}{3}\alpha\rho\nabla \cdot \mathbf{u}k\right) - \left(\alpha\rho\frac{\epsilon}{k}k\right) + S_k + S_{fvOptions} \tag{17}$$

where $G$ is the turbulent kinetic energy production rate due to the anisotropic part of the Reynolds-stress tensor ($\mathrm{m}^2\ \mathrm{s}^{-3}$), $D_\epsilon$ is the effective diffusivity for $\epsilon$, $C_1$ (s) and $C_2$ are two model coefficients, $C_{3,RDT}$ is the rapid-distortion theory compression term coefficient, $S_\epsilon$ is the internal source term for $\epsilon$, $S_{fvOptions}$ are source terms introduced by fvOptions dictionary for $\epsilon$, $S_k$ is the internal source term for $k$ and $S_{fvOptions}$ are source terms introduced by fvOptions dictionary for $k$.

In Equations 13, 14, 16 and 17, phase indicator $\alpha_i$ is defined as follows:

$$\alpha_i(x,t) = \begin{cases} 1 & \text{if phase } i \text{ is present at } x,t \\ 0 & \text{else} \end{cases} \tag{18}$$

and is calculated in a volumetric phase fraction equation:

$$\frac{\partial \alpha_i}{\partial t} + \nabla \cdot (\alpha_i \mathbf{u}) + \sum_j \nabla \cdot (\alpha_i \alpha_j \mathbf{u}_{r,ij}) = 0 \tag{19}$$

where $\mathbf{u}_{r,ij}$ is the relative velocity between phases.

The following default values were used:

$$C_\mu = 0.09; C_1 = 1.44; C_2 = 1.92; C_{3,RDT} = 0$$

Here we use the multiphaseInterFoam solver with three viscous fluids, the air, the water and the landslide and the PIMPLE algorithm which combines PISO (Pressure Implicit with Splitting of Operator) and SIMPLE (Semi-Implicit Method for Pressure-Linked Equations). Cartesian grids are generated by blockMesh and refined by snappyHexMesh using triangular elements in the area along the slope. The landslide is modeled as a Newtonian non-miscible fluid. Python scripts are used to postprocess the results (local free surface time series, cross-sectional views of the landslide).

In Sections 3.2 and 3.3, and consistently with the depth-averaged model, the solver is used in laminar mode ($\mu_t = 0$ in Equation 12). This allows to focus the comparison on the main difference between the two models, namely flow depth-averaged (AVALANCHE) or fully resolved (OpenFOAM). Further, in Section 3.4, the influence of the turbulence is studied, considering a $k - \epsilon$ model in the Navier-Stokes model.

# 3 Simulations

We focus on two laboratory experiments to validate both models: a subaerial landslide (Viroulet et al. 2016) and a submerged one (Grilli et al. 2017), both deformable (Figure 1).

## 3.1 Benchmarks description

*Subaerial case*

The experiment described in Viroulet et al. (2016) involves a subaerial landslide composed of 0.0015 m diameter glass beads, contained in a 0.11 m high isosceles right-angled triangle by a vertical polyvinyl plate. The density of the beads is 2000 kg $m^{-3}$ but the equivalent density of the slide (air and beads) is 1500 kg $m^{-3}$. Once the plate is raised, the beads collapse on a 45° slope into 0.15 m of water, in a 2.20 m long, 0.4 m high and 0.2 m wide tank. The evolution of the collapse is recorded by a high speed camera (100 frames

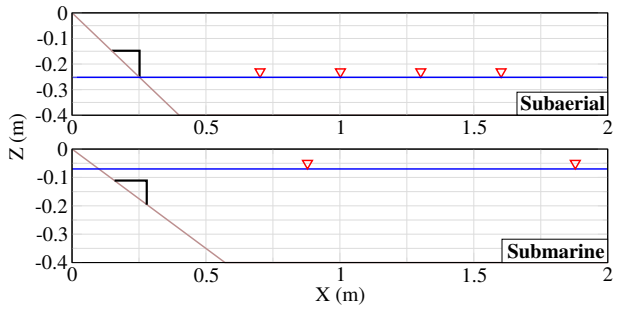


Figure 1: Geometry and gauges locations for the subaerial (gauges at x=0.702, 1.002, 1.302 and 1.602 m, top panel) and submerged (gauges at x=0.879 and 1.879 m, bottom panel, and x=2.879 and 3.879 m, not visible here) benchmarks (Viroulet et al. 2016, Grilli et al. 2017). In both panels, the slide is represented in black, the slope in brown, the water in blue and the gauges with the red triangles.

per second). The evolution of the generated water waves is recorded by four resistive gauges located at 0.45, 0.75, 1.05 and 1.35 m from the plate.

Ionescu et al. (2015) proposed an approximation to evaluate the viscosity of the equivalent fluid following the $\mu(I)$-rheology during the initial phase of sliding. Following this idea, Clous & Abadie (2019) found for this benchmark a value of 12.8 Pa.s, which will be used here in the simulations.

*Submerged case*

The experiment described in Grilli et al. (2017) involves a submerged landslide composed of 0.004 m diameter glass beads, contained in a 0.12 m long, 0.085 m high right-angled triangle by a sluice gate. The density of the beads is 2500 kg m$^{-3}$ leading to an equivalent density of 1951 kg m$^{-3}$. The collapse occurs on a 35° slope into 0.33 m of water, in a 6.27 m long and 0.25 m wide tank. In a similar way to the subaerial experiment, a high speed camera (1000 fps) records the landslide evolution, while gauges located at 0.6, 1.6, 2.6 and 3.6 m of the gate record the water waves time series.

Geometry and gauges locations of both cases are represented in Figure 1 (top panel for the subaerial benchmark, bottom panel for the submerged one).

## 3.2 Benchmarks simulations

*Depth-averaged model*

For both subaerial and submerged benchmarks, a sensitivity analysis is carried out to determine the effect of the viscosity $\mu$ in the range [0.01; 40] Pa.s. All the simulations are performed in a 1D cartesian grid of 0.001 m resolution in the x-direction. A convergence study was performed and the results did not show any significant differences between this resolution and a finer one. As in the experiment, a reflective right boundary condition is used for the submerged case. First of all, full shallow water simulations are computed to evaluate how fast the first generated wave separates from the slide. When the wave is considered to be not affected anymore by the landslide, we switch from shallow water equations to Boussinesq equations.

*Navier-Stokes model*

For both landslides, the $(x, z)$ 0.005 m resolution mesh generated by blockMesh is refined on one layer

along the slopes and the bottom with triangular elements by snappyHexMesh. The resolution in $x$ is coarser than that of the depth-averaged model due to the higher computational cost, but it is nevertheless sufficient to ensure convergence. For both benchmarks, pseudo 3D grids are composed of one cell in the transversal y-direction. Sensitivity studies are conducted on the viscosity $\mu$ (with values in the range [0.01; 50] Pa.s) and the lowerWall (slope and bottom) boundary condition (*i.e.* noSlip and partialSlip). The latter is defined through a coefficient $\alpha$ between 0 and 1. If $u_0$ is the tangential velocity on the wall and $u_1$ the tangential velocity of the adjacent cell, $\alpha$ is defined as follows: $u_0 = (1-\alpha)u_1$, $\alpha$ being defined as $\alpha = d/(d+2\lambda)$ where $\lambda$ is the slip length and $d$ the cell size. With these definitions, a noSlip boundary condition corresponds to a $\alpha$ value of 1. In the following, a 0.1 partialSlip condition will refer to a partialSlip condition with $\alpha$=0.1.

*Analysis*

The comparison of the free surface signals obtained from the simulations ($f_1$) and the experiments ($f_2$) is carried out based on the Q parameter, built on Sobolev norms (Perlin & Bustamante 2016):

$$Q(f_1, f_2) = \frac{\left(\int |F_1(\omega) - F_2(\omega)|^2 d\omega\right)^{1/2}}{\left(\int |F_1(\omega)|^2 d\omega\right)^{1/2} + \left(\int |F_2(\omega)|^2 d\omega\right)^{1/2}} \tag{20}$$

where $f_1$, $f_2$ are the two temporal signals and $F_1(\omega)$, $F_2(\omega)$ the associated Fourier transforms.

This parameter $Q$ gives a measure of the phase shift of the two signals. For identical time series, $Q$=0, whereas $Q$=1 for two ideal (sinusoidal) signals separated by a half-period (e.g. $sin(x)$ and $sin(x+\pi)$).

As regards the landslide evolution, comparisons between simulations and experiments are made in a qualitative way simply by overlapping simulated and observed snapshots of slice views of the landslide at different instants.

### 3.3 Sensitivity studies on the landslide characteristics

The simulation of the two benchmarks and the comparison with the data allow to select a set of optimal parameters for each code (viscosity, type of equations for the depth-averaged model, slip condition for the Navier-Stokes model). These parameters will then be used in a sensitivity study consisting in varying the slope and the submergence considered in the first benchmark (Figure 2), keeping the same shape, volume, gauges locations and water depth (*i.e.*, a triangle, 0.00605*1 $m^3$, x=0.702, 1.002, 1.302, 1.602 and 0.15 m, respectively).

In the sensitivity study, simulations are performed with slope angles ranging from 20 to 60° with 5° step. Considering the reference point for the submergence as the foot of the landslide, we also tested five values of relative submergences S from -1 to +1, a submergence $S_{+1}$ being a raise of one landslide length along the slope (Figure 2). The initial geometry of the subaerial benchmark does not allow to simulate a submergence deeper than -1 without changing the water depth.

We chose to keep the same volume for all the simulations. Therefore, the portion of slide under water is not identical for submerged cases and different slopes. Consequently, comparing a same submergence for

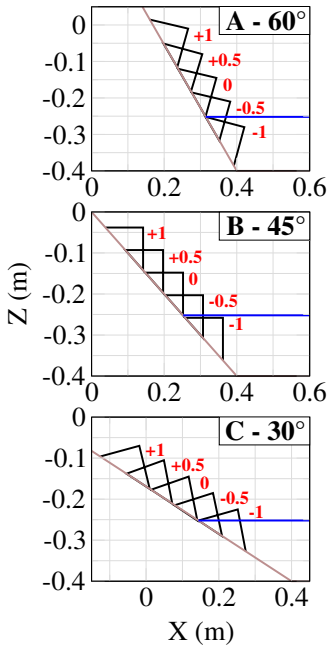


Figure 2: Initial slides positions (in black) for slopes (in brown) of 60° (A), 45° (B) and 30° (C) and different relative submergences ($S_{-1}$, $S_{-0.5}$, $S_0$, $S_{+0.5}$ and $S_{+1}$, in red). The blue line is the initial water surface.

different slope angles will be delicate and we can only study the influence of the submergence for a given slope.

### 3.4 Sensitivity study on the turbulence

Now, we propose to show the influence of the turbulence modeling basically by turning on and off a $k-\epsilon$ model (same as Rauter et al. (2021)) in the Navier-Stokes simulations. As shown in the previous part, the molecular viscosities required in the slide for the simulations to compare favorably with granular experiments are quite high and the slide Reynolds numbers correspondingly low. Therefore, the turbulence should be quite limited in the slide but plays a role in water and at the interface between the slide and water. Nine cases have been simulated with the Navier-Stokes model in both laminar and turbulent modes to investigate the influence of $k-\epsilon$ involving the slope angles of 35, 45 and 60°, three submergences ($S_{-1}$, $S_0$ and $S_{+1}$) with $Re_s \sim 20$ (in laminar cases).

### 3.5 Dimensionless variables

The analysis of the results of the sensitivity studies is performed using the following dimensionless variables:

- The dimensionless wave amplitude $H/h$ where $H$ is the amplitude of the wave and $h$ the water depth (over the flat bottom part).
- The dimensionless velocity $V_s/V_0$ where $V_s$ is the landslide velocity and $V_0 = \sqrt{2gd_0}$ a characteristic velocity with $d_0$ the landslide thickness at t=0 s. $V_0$ approximates the initial fluid velocity appearing in the bottom part of the slide (here considering no energy loss).

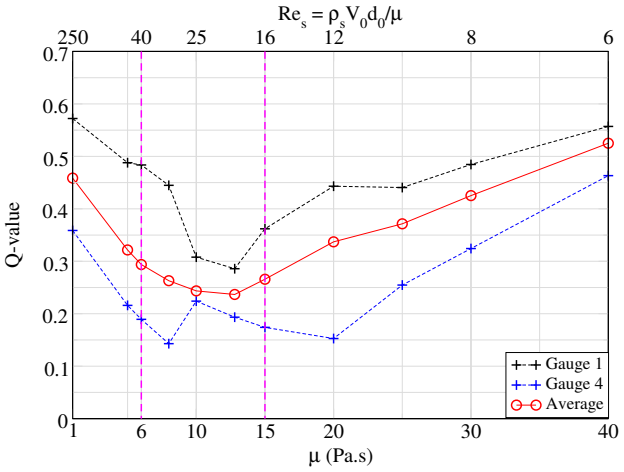


Figure 3: Subaerial benchmark: Q-values calculated for surface elevation time series from the depth-averaged model as functions of the viscosity $\mu$ (Pa.s) at Gauges 1 (black) and 4 (blue). Red curve represents the average Q-value for the four gauges. Pink lines define a zone where results are considered satisfactory in average.

The landslide viscosity $\mu$ is linked to the Reynolds number through the following relationship:

$$Re_s = \frac{\rho_s V_0 d_0}{\mu} \tag{21}$$

where $\rho_s$ is the landslide density.

# 4 Results

As indicated in Section 3.2, we recall that the following results were obtained by simulations involving a combination of shallow water and Boussinesq models.

## 4.1 Subaerial case

### 4.1.1 Depth-averaged model

*Water waves*

Figure 3 shows that the best average Q-value for the four gauges is obtained with a viscosity $\mu$ of 12.8 Pa.s. This value corresponds to the $\mu(I)$-rheology viscosity calculated by Clous & Abadie (2019) following Ionescu et al. (2015). In a general way, in the "far-field" (Gauge 4), Q-values are lower than those in the "near-field" (Gauge 1), showing that the depth-averaged model is more accurate in the far-field.

For viscosity values between 6 and 15 Pa.s, results are similar with low Q-values. This is illustrated by the analysis of the free surface elevation time series at the four gauges (Figure 4) which shows similar results, close to the experimental water waves whatever the viscosity taken in this range. Nevertheless, we note that if the characteristics of the leading wave (period and height) are reproduced accurately, the fit is lower for the following water waves.

*Landslide*

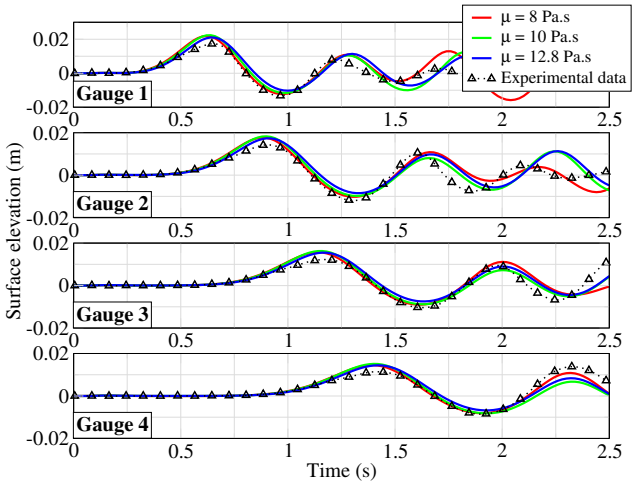


Figure 4: Subaerial benchmark: comparison of surface elevation time series between the experiments (black triangles) and the depth-averaged model simulations using slide viscosity $\mu$ of 8 Pa.s (red), 10 Pa.s (green) and 12.8 Pa.s (blue).

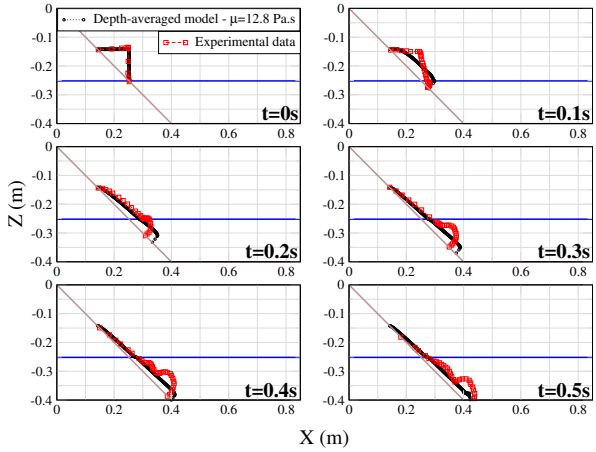


Figure 5: Subaerial benchmark: comparison of slide contours between experiments (red squares) and the depth-averaged model simulation with $\mu$=12.8 Pa.s (black circles). From left to right and up to down, contours are represented every 0.1 s from t=0 to t=0.5 s. The blue line represents the initial water surface. The brown line represents the slope.

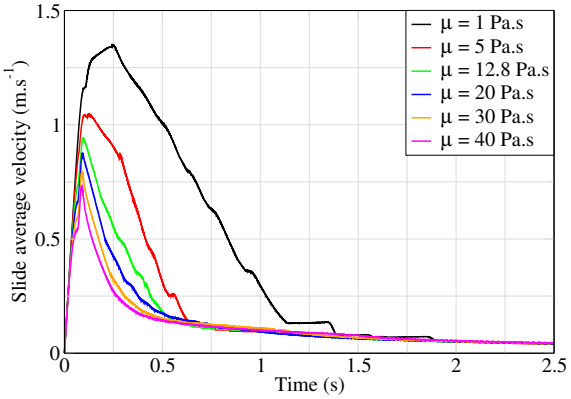


Figure 6: Subaerial benchmark: evolution of the average landslide velocity during the depth-averaged model simulation as a function of the viscosity ($\mu$ ranging from 1 to 40 Pa.s).

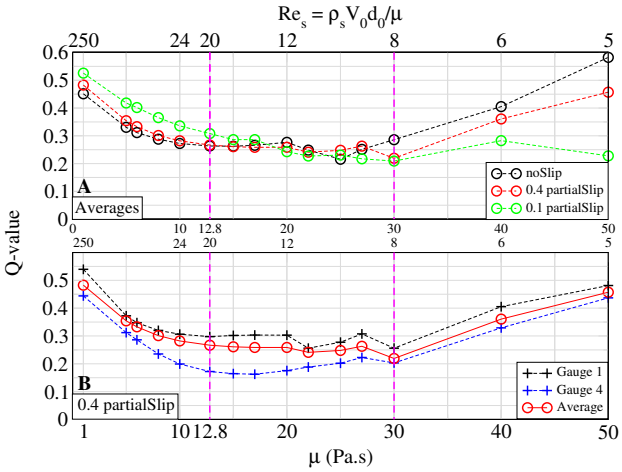


Figure 7: Subaerial benchmark: Q-values calculated for surface elevation time series from the Navier-Stokes model as functions of the viscosity $\mu$ (Pa.s). **A**. Average Q-values for the four gauges calculated using the three slip boundary conditions (noSlip (black), 0.4 partialSlip (red) and 0.1 partialSlip (green)). **B**. Q-values calculated for Gauges 1 (black) and 4 (blue) and average Q-values for the four gauges (red) using the 0.4 partialSlip condition.

Considering the landslide itself, the simulation with a viscosity value $\mu$ of 12.8 Pa.s gives satisfactory results, as shown in Figure 5. Due to the landslide model hypothesis, the experimental front shape is not properly reproduced but the quantity of material entering into the water at different times is very similar in the simulation and in the experiment. Moreover, as shown by Clous & Abadie (2019), most of the energy transfer between the landslide and the wave occurs within the first instants (before t=0.3s) in this case, so it is not essential to reproduce perfectly the landslide behavior afterward to properly simulate the water waves generated.

For lower and higher values of viscosity, Q-values increase, probably due to incorrect landslide velocities, as supported by Figure 6, which illustrates the variety of the average slide velocity observed in the simulations.

### 4.1.2 Navier-Stokes model

*Water waves*

Figure 7A highlights the existence of a plateau between viscosity values of 12.8 and 30 Pa.s (pink lines) where Q-values are satisfactory. Note that similar values are obtained for the three tested boundary conditions in this viscosity range.

Before the plateau, the noSlip condition gives better results (lower Q-values) whereas best values are obtained after the plateau for the 0.1 partialSlip condition. This stresses the importance of the slide average velocity at the beginning of the process which is controlled both by viscosity and bottom boundary condition.

Figure 8 shows indeed that different combinations of viscosity values and boundary conditions give similar results regarding the leading wave.

Figure 7B shows that, as for the depth-averaged model, Q-values in the far-field (Gauge 4) are lower than those computed in the near-field (Gauge 1).

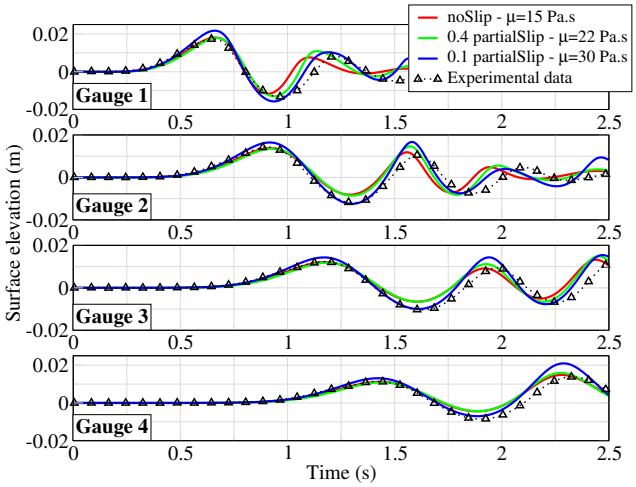


Figure 8: Subaerial benchmark: comparison of surface elevation time series (m) between the experiments (black triangles) and the Navier-Stokes model simulations using viscosity $\mu$ of 15 Pa.s with a noSlip boundary condition (red), 22 Pa.s with a 0.4 partialSlip condition (green) and 30 Pa.s with a 0.1 partialSlip condition (blue).

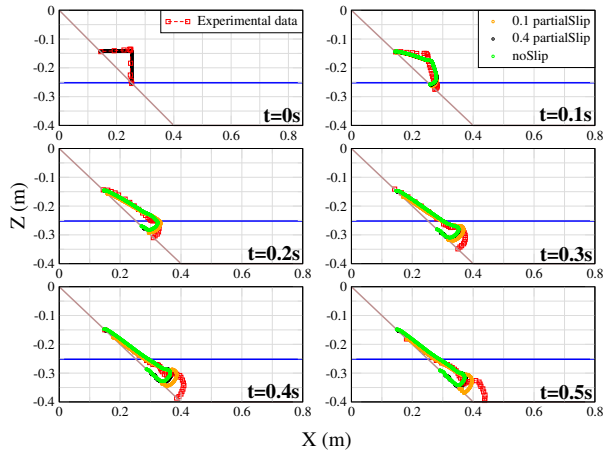


Figure 9: Subaerial benchmark: comparison of slide contours between experiments (red squares) and the Navier-Stokes model simulations with $\mu$=12.8 Pa.s and noSlip (green), 0.4 partialSlip (black) or 0.1 partialSlip (orange) slip conditions. From left to right and up to down, contours are represented every 0.1 s from t=0 to t=0.5s. The blue line represents the initial water surface. The brown line represents the slope.

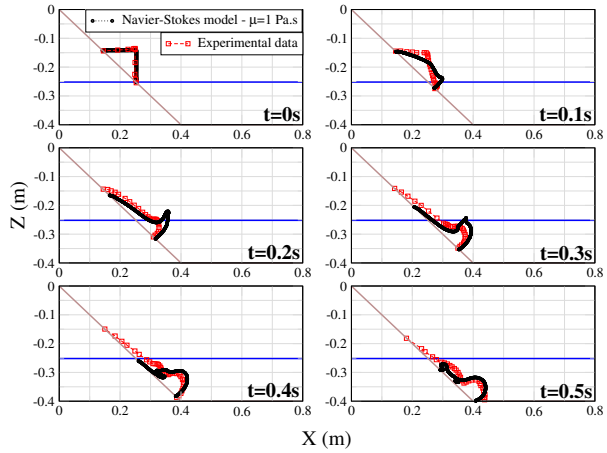


Figure 10: Subaerial benchmark: comparison of slide contours between experiments (red squares) and the Navier-Stokes model simulations with $\mu$=1 Pa.s and 0.1 partialSlip (black) slip condition. From left to right and up to down, contours are represented every 0.1 s from t=0 to t=0.5s. The blue line represents the initial water surface. The brown line represents the slope.

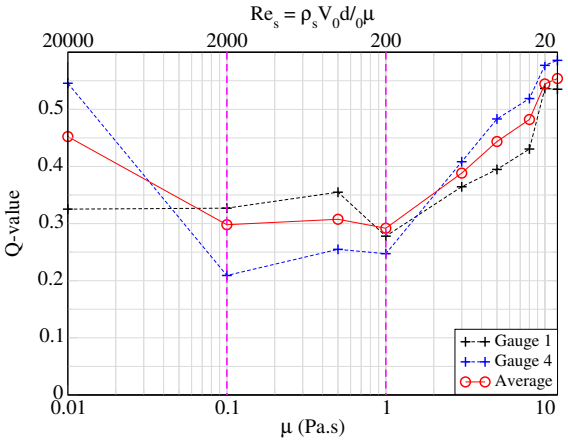


Figure 11: Submerged benchmark: Q-values calculated for surface elevation time series from the depth-averaged model as functions of the viscosity $\mu$ at Gauges 1 (black) and 4 (blue). Red curve represents the average Q-value for the four gauges. Pink lines define a zone where results are considered satisfactory in average. X-axis is logarithmic.

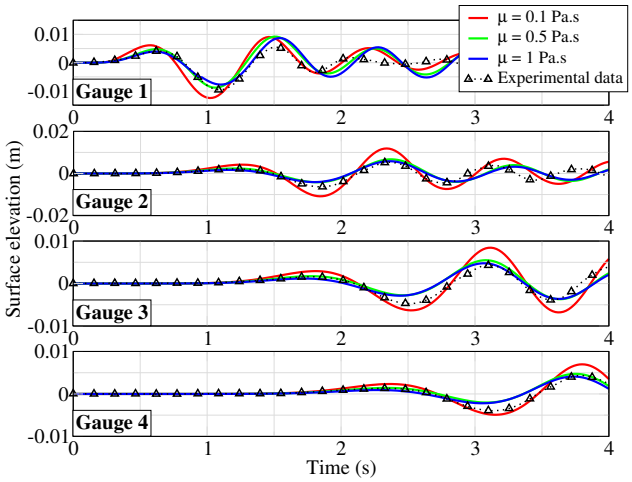


Figure 12: Submerged benchmark: comparison of surface elevation time series (m) between the experiments (black triangles) and the depth-averaged model simulations using a viscosity $\mu$ of 0.1 Pa.s (red), 0.5 Pa.s (green) and 1 Pa.s (blue).

*Landslide*

With a viscosity of 12.8 Pa.s, the slide kinematics is only correct up to t=0.2s (Figure 9). After this time, the landslide is too slow independently of the bottom boundary condition. This behavior differs from the one obtained with the depth-averaged model (Figure 5). To reproduce the experimental landslide behavior with the Navier-Stokes model, at least the overall trajectory of the gravity center, a viscosity value $\mu$ of 1 Pa.s with a 0.1 partialSlip boundary condition (Figure 10) has to be used, but in this case the landslide front is too large, producing incorrect waves (more than two times larger that the experimental data).

## 4.2 Submerged case

### 4.2.1 Depth-averaged model

*Water waves*

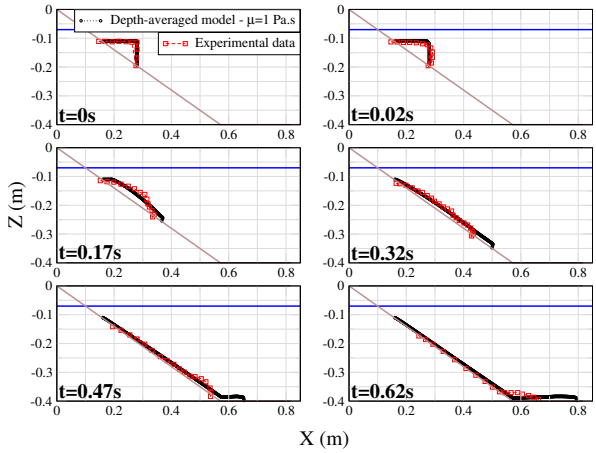


Figure 13: Submerged benchmark: comparison of slide contours between experiments (red squares) and the depth-averaged model simulation with $\mu$=1 Pa.s (black circles). From left to right and up to down, contours are represented at t=0, 0.02, 0.17, 0.32, 0.47 and 0.62 s. The blue line represents the initial water surface. The brown line represents the slope.

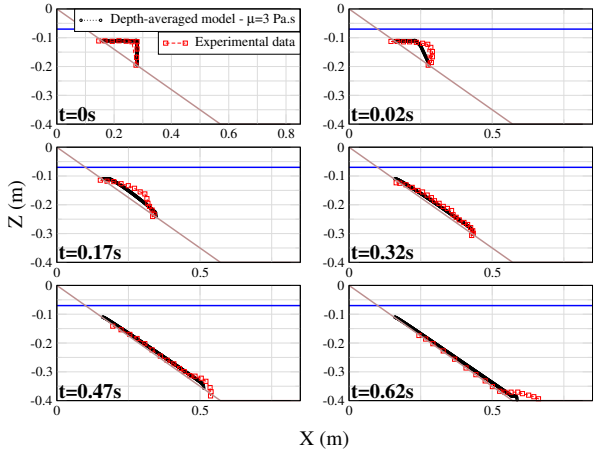


Figure 14: Same as Figure 13 for $\mu$=3 Pa.s.

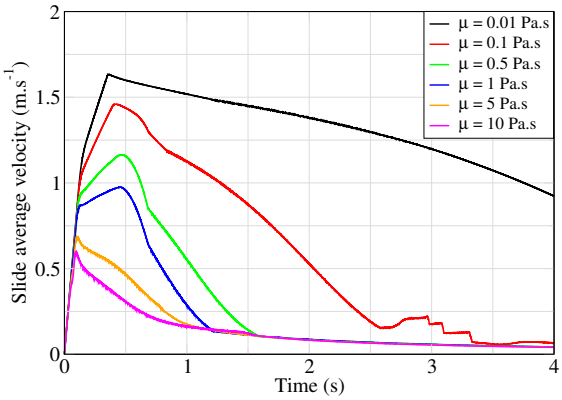


Figure 15: Submerged benchmark: evolution of the average landslide velocity during the depth-averaged model simulation as a function of the viscosity $\mu$ ranging from 0.01 to 12 Pa.s.

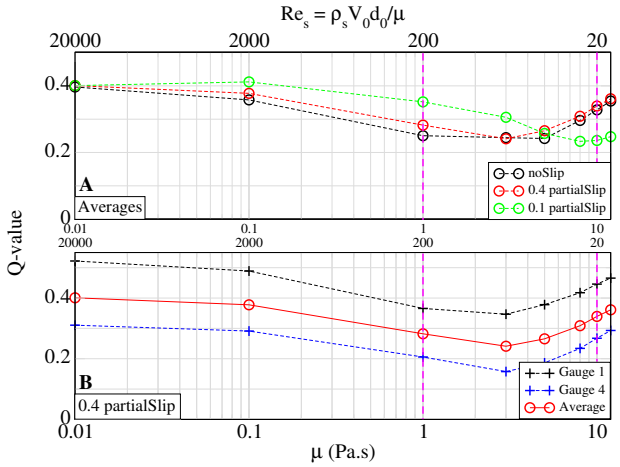


Figure 16: Submerged benchmark: Q-values calculated for surface elevation time series from the Navier-Stokes model as functions of the viscosity $\mu$. **A**. Average Q-values for the four gauges calculated using the three slip boundary conditions (noSlip (black), 0.4 partialSlip (red) and 0.1 partialSlip (green)). **B**. Q-values calculated for Gauges 1 (black) and 4 (blue) and average Q-values for the four gauges (red) using the 0.4 partialSlip condition. X-axis is logarithmic.

In the submerged landslide case, the same shape for the Q-values curve as that of the subaerial benchmark is observed, a trough and a plateau of optimal viscosity. The best performances are obtained with viscosity values between 0.1 and 1 Pa.s (Figure 11). Overall, considering the four gauges, a viscosity of 1 Pa.s gives the best results.

Surface elevations are globally well reproduced using a viscosity value $\mu$ between 0.1 and 1 Pa.s (Figure 12). This is especially true for the first wave, the next waves being slightly too high compared to the experiments, especially at Gauge 1 (top panel in Figure 12).

*Landslide*

With $\mu$=1 Pa.s (Figure 13), the simulated landslide matches the experimental data up to t=0.17s (middle left panel, Figure 13) and deviates afterward due to larger velocities. With $\mu$=3 Pa.s, the landslide behavior is better reproduced (Figure 14), the simulation being close to the experimental data up to t=0.47s (bottom left panel).

Figure 15 shows times landslides touch the bottom and start to slow down in cases $\mu$=0.01, 0.1, 0.5 and 1 Pa.s (peaks of corresponding lines in Figure 15) whereas for $\mu$=5 or 10 Pa.s, the landslide starts to slow down before reaching the bottom which likely affects waves generation.

### 4.2.2 Navier-Stokes model

*Water waves*

Figure 16A shows again that optimal results are similarly obtained for the noSlip and 0.4 partialSlip conditions at viscosity values between 1 and 5 Pa.s. While with the 0.1 partialSlip condition, best Q-values are obtained for higher viscosity values. Considering the 0.4 partialSlip condition (Figure 16B), the best results are obtained with a viscosity value of 3 Pa.s. Moreover, as previously seen, waves are better

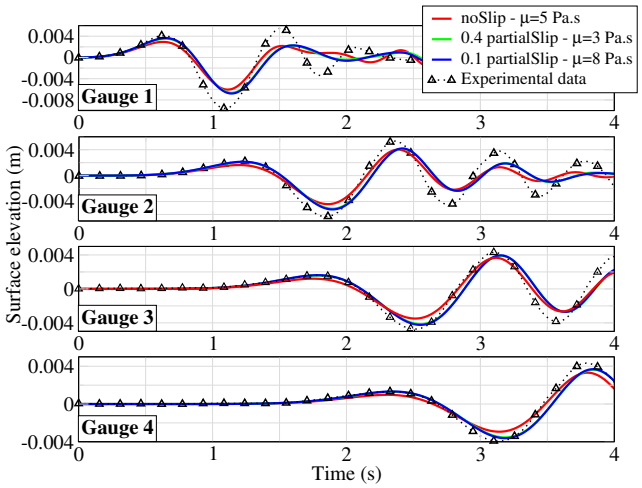


Figure 17: Submerged benchmark: comparison of surface elevation time series (m) between the experiments (black triangles) and the Navier-Stokes model simulations using viscosity $\mu$ of 5 Pa.s with a noSlip boundary condition (red), 3 Pa.s with a 0.4 partialSlip condition (green) and 8 Pa.s with a 0.1 partialSlip condition (blue).

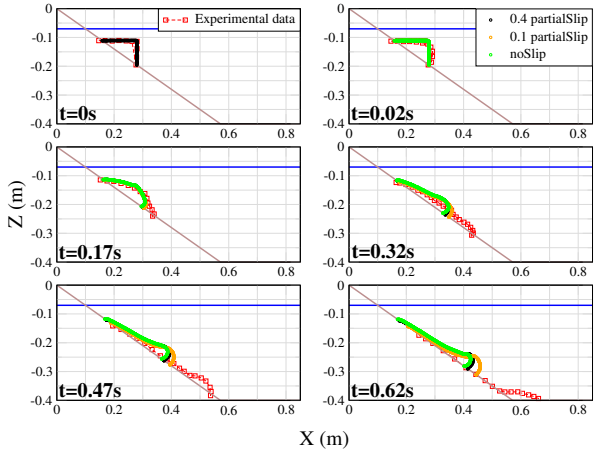


Figure 18: Submerged benchmark: comparison of slide contours between experiments (red squares) and the Navier-Stokes model simulations with $\mu$=3 Pa.s and noSlip (green), 0.1 partialSlip (orange) or 0.4 partialSlip (black) slip conditions. From left to right and up to down, contours are represented at t=0, 0.02, 0.17, 0.32, 0.47 and 0.62 s. The blue line represents the initial water surface. The brown line represents the slope.

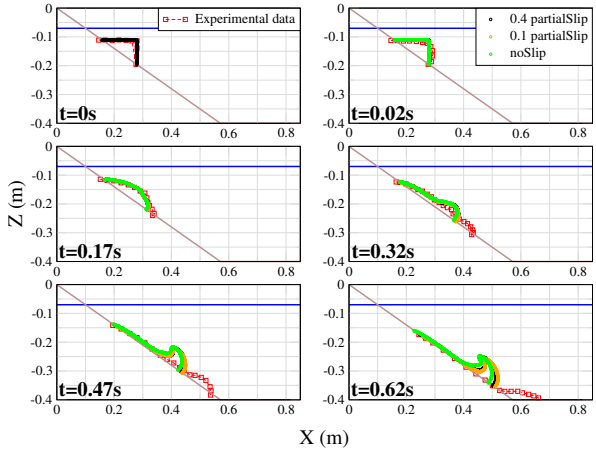


Figure 19: Same as Figure 18 with $\mu$ = 0.1 Pa.s.

reproduced in the far-field than the near-field.

Figure 17 presents the comparison between the Navier-Stokes model simulations and the experimental data for the three best combination of parameters (*i.e.*, viscosity value and bottom boundary condition). Surprisingly, the behavior of the model is very similar at the four gauges whatever the combination. At Gauge 1 (top panel), the peak of the first wave is well reproduced whereas the following waves are attenuated. The latter are better reproduced on the three other gauges. Hence, to generate the same wave, a full slip condition (0.1 partialSlip) requires a higher viscosity value ($\mu$=8 Pa.s) than a medium slip condition (0.4 partialSlip, $\mu$=3 Pa.s) or a noSlip condition ($\mu$=5 Pa.s).

*Landslide*

Although simulations with the following combination (0.4 partialSlip and $\mu$=3 Pa.s) give good results regarding the waves, they do not reproduce the landslide correctly (Figure 18). A lower viscosity value ($\mu$=0.1 Pa.s) is actually needed to better reproduce the landslide motion at the first instants (*i.e.*, until t=0.17 s in Figure 19). Beyond t=0.17 s, even a quasi full slip condition (*i.e.*, 0.1 partialSlip, in orange) is not sufficient to reach the position of the experiment slide front. The difference along the slope between the observed and the simulated locations of the landslide front increases progressively and reaches 7.2 cm at t=0.32 s and about 17 cm at t=0.62 s (Figure 19). The difference observed could be explained by the absence of water incorporation within the landslide.

Additionally, whatever the viscosity value and regardless of the boundary condition at the bed, a 5-10 cm high flow front forms slowing down the whole landslide.

### 4.3 Sensitivity studies on the landslide characteristics

This section presents a sensitivity analysis aiming at better understanding the influence of the slope angle and the landslide submergence, on the first generated wave amplitude. The main objective is to define the sets of parameters for which both models give similar results and the ones leading to differences. Results are presented in dimensionless variables (see Section 3.5 which introduces the landslide Reynolds number $Re_s$).

The viscosity in each model has been chosen so that the first water wave is similar in both models and close to the two previous experimental data. This is achieved with: a $Re_s \sim 20$ ($\mu$=12.8 Pa.s) (and a 0.4 partialSlip condition for the Navier-Stokes model). We also decided to include a second Reynolds number closer to the one used in our submerged benchmark simulations: $Re_s \sim 250$ ($\mu$=1 Pa.s).

With the depth-averaged model, the following results are obtained (Figure 20):

- For both Reynolds values, the higher the slope angle, the larger the first generated wave, following quasi linear relationships.
- For any slope angles and for both Reynolds, when the landslide starts near or just above the water surface (submergences $S_{-0.5}$ and $S_0$) the generated wave is larger than with the other submergences tested. Submergences $S_{-0.5}$ and $S_0$ give very similar results, except from 50° for $Re_s \sim 250$.

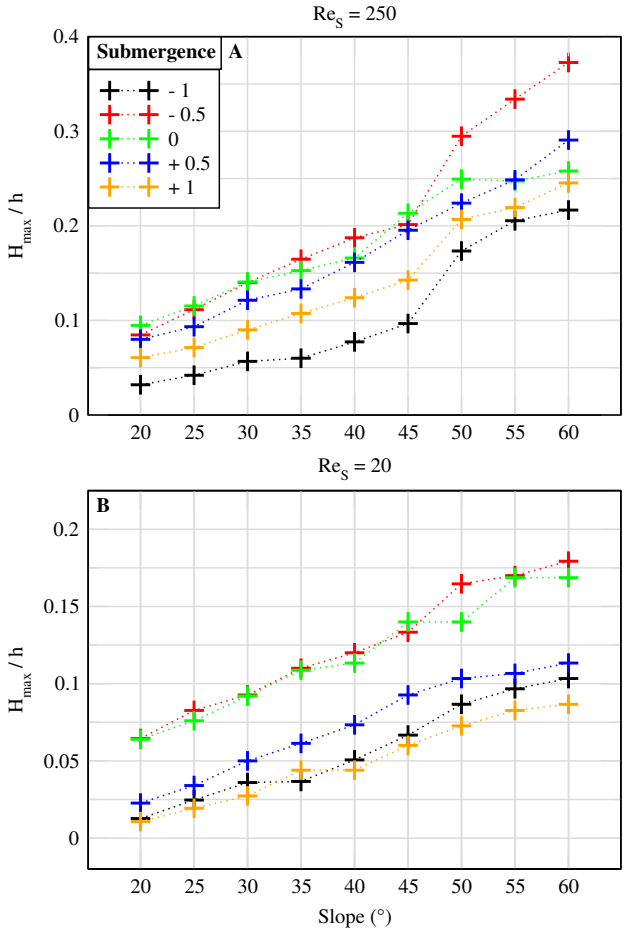


Figure 20: Amplitude of the first wave (m), measured at Gauge 1, as a function of the slope angle (in degree) for the depth-averaged model, five submergences ($S_{-1}$ in black, $S_{-0.5}$ in red, $S_0$ in green, $S_{+0.5}$ in blue and $S_{+1}$ in orange) and two slide Reynolds numbers $Re_s$: 250 (A) and 20 (B).

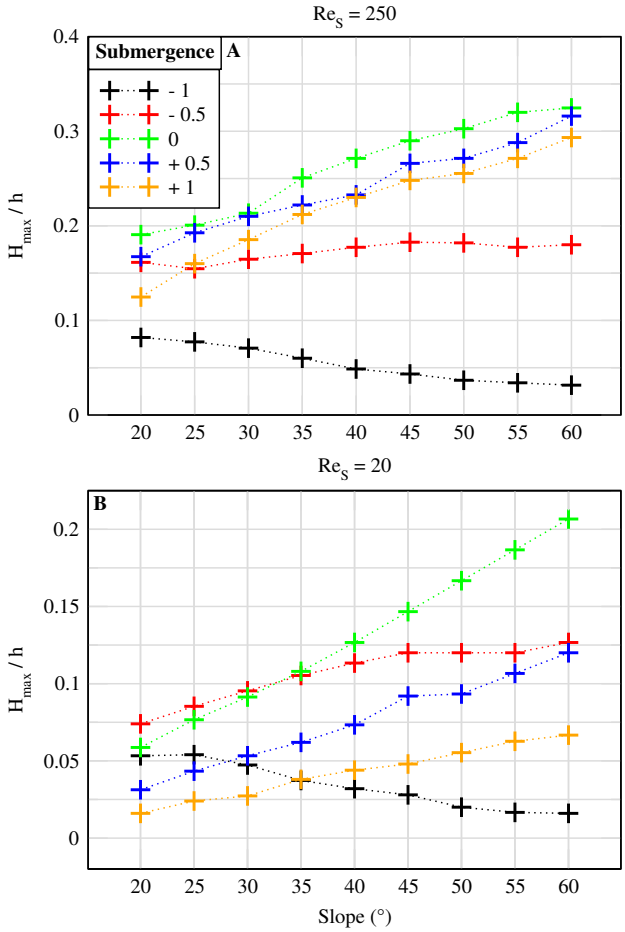


Figure 21: Amplitude of the first wave (m), measured at Gauge 1, as a function of the slope angle (in degree) for the Navier-Stokes model, five submergences ($S_{-1}$ in black, $S_{-0.5}$ in red, $S_0$ in green, $S_{+0.5}$ in blue and $S_{+1}$ in orange) and two slide Reynolds numbers $Re_s$: 250 (A) and 20 (B).

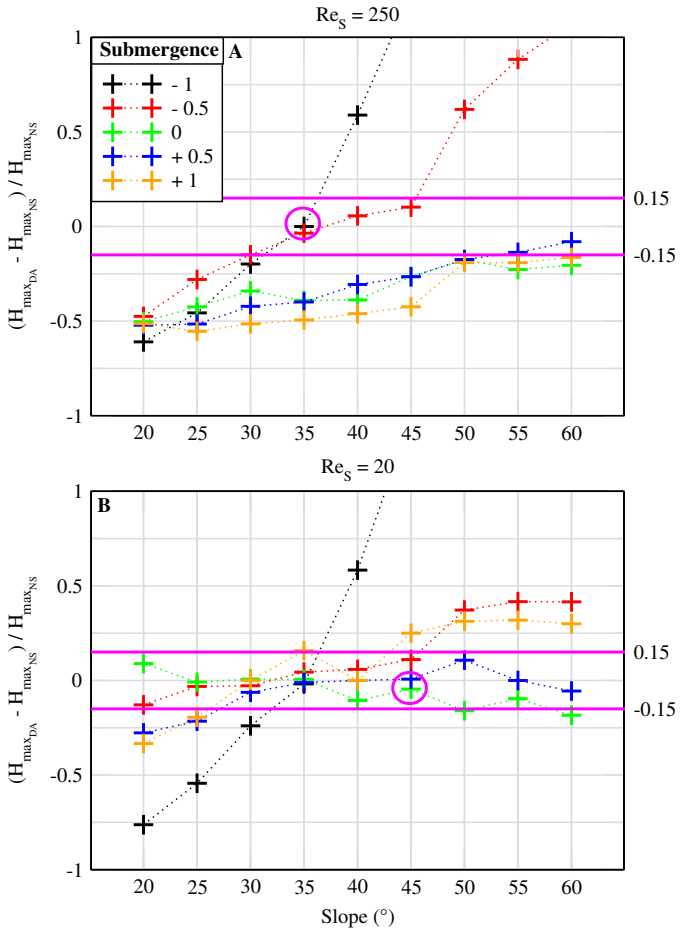


Figure 22: Computed difference for the amplitude of the first wave between the depth-averaged (DA) model and the Navier-Stokes (NS) model (reference) as a function of the slope angle (°) for Reynolds numbers of 250 ($\mu$=1 Pa.s, A) and 20 ($\mu$=12.8 Pa.s, B) and for submergences $S_{-0.5}$ (red), $S_0$ (green), $S_{+0.5}$ (blue) and $S_{+1}$ (orange). Horizontal pink lines mark an interval of ± 15% within which results with both models are considered similar. Pink circles correspond to the cases the closest to the benchmarks simulated in Sections 4.2 (A) and 4.1 (B).

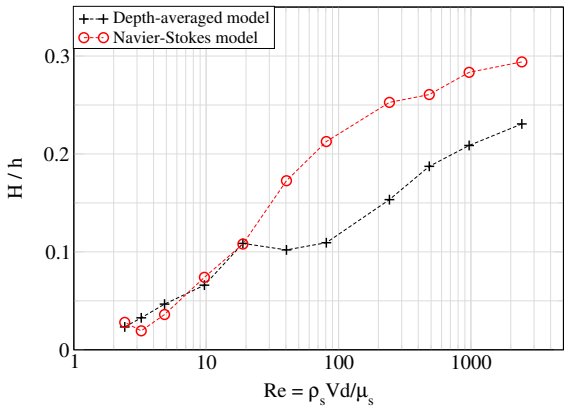


Figure 23: Dimensionless maximal water wave amplitude computed by the depth-averaged model (black) and the Navier-Stokes model (red) as a function of the slide Reynolds number. The submergence is $S_0$ and the slope 35°.

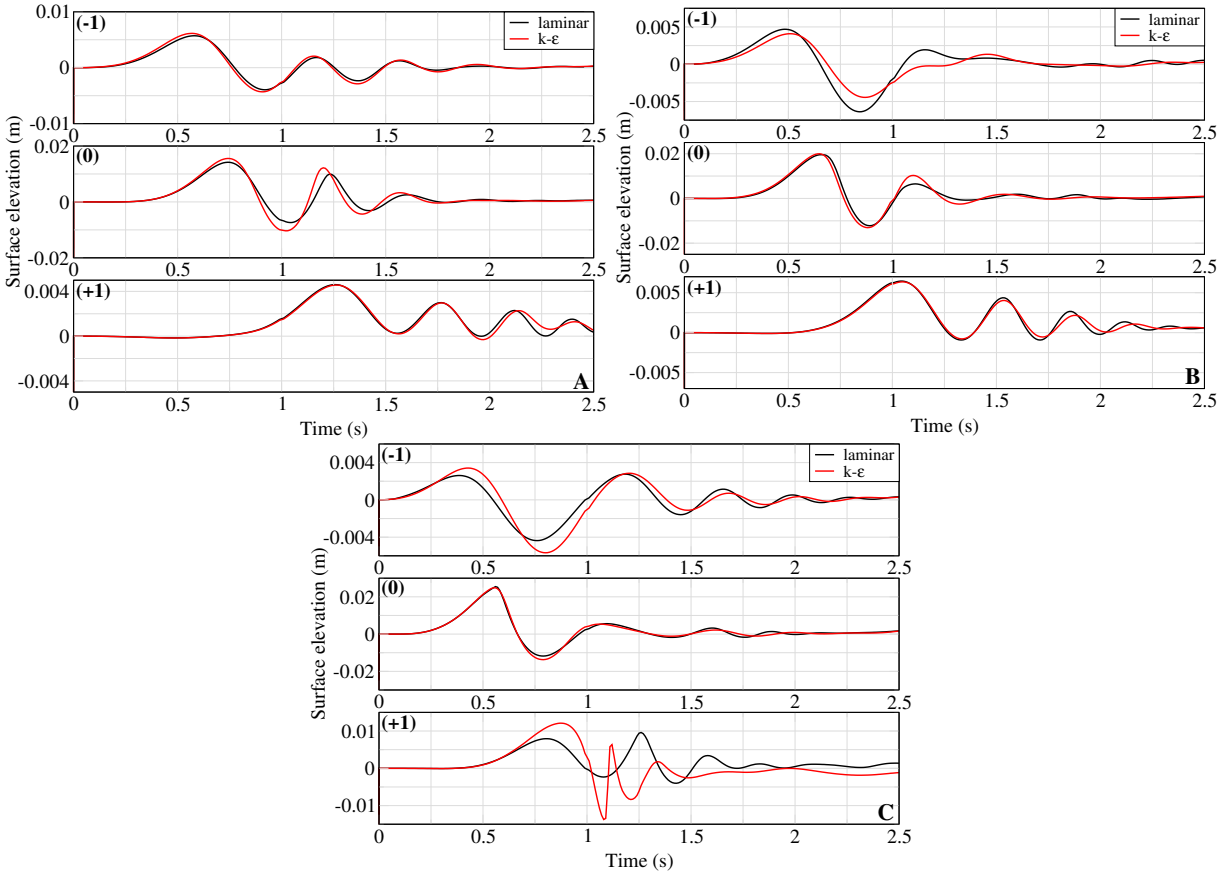


Figure 24: Comparison of surface elevation time series (m) between laminar (black) and $k-\epsilon$ (red) simulations with the Navier-Stokes model using $Re_s \sim 20$ with a noSlip boundary condition for submergences $S_{-1}$ (top panels), $S_0$ (middle panels) and $S_{+1}$ (bottom panels) and for slope angles of 35° (A), 45° (B) and 60° (C).

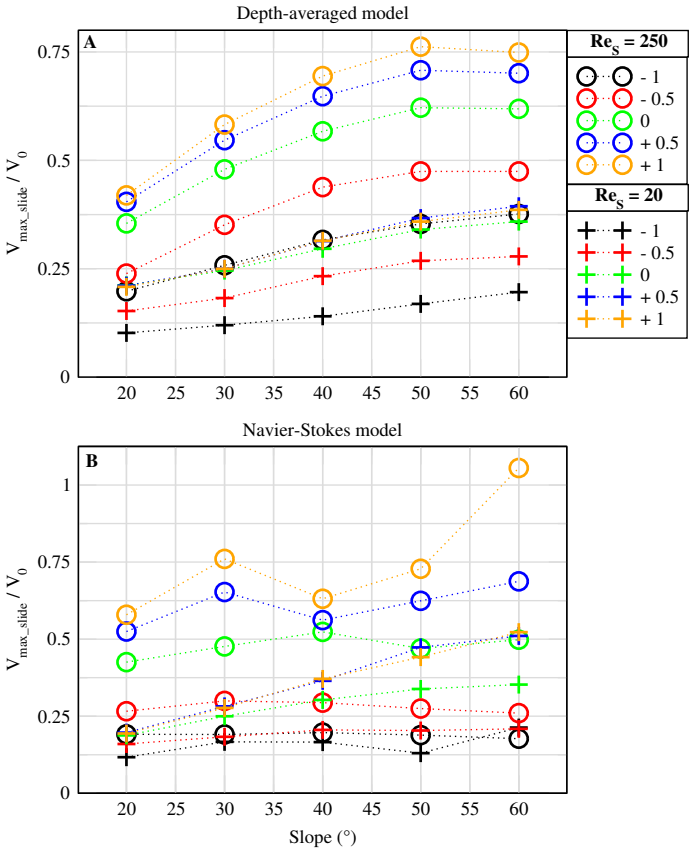


Figure 25: Landslide velocity (m.s$^{-1}$) as a function of the slope angle (in degree) for the depth-averaged model (A) and the Navier-Stokes model (B), five submergences ($S_{-1}$ in black, $S_{-0.5}$ in red, $S_0$ in green, $S_{+0.5}$ in blue and $S_{+1}$ in orange) and two Reynolds numbers $Re_s$: 20 (plus) and 250 (circles).

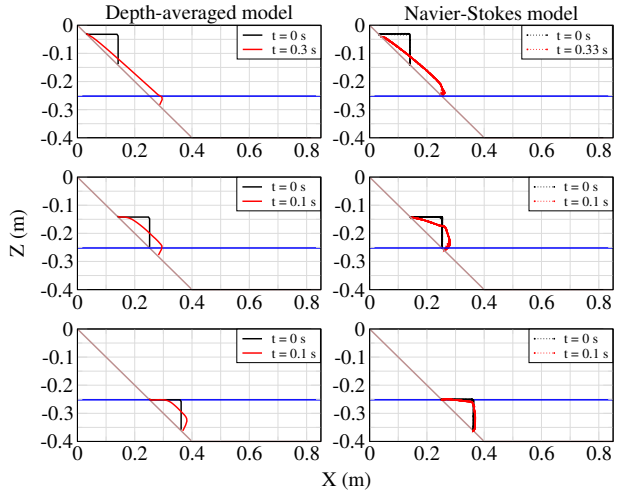


Figure 26: Snapshots of initial (in black) and entering or just entered into the water (in red) landslides for a slope angle of 45° and three submergences, $S_{+1}$ (top panels), $S_0$ (middle panels) and $S_{-1}$ (bottom panels), for the depth-averaged model (left panels) and the Navier-Stokes model (right panels) and $Re_s$ ∼20. The blue line represents the initial water surface. The brown line represents the slope.

- With the large slide Reynolds number $Re_s$ (250), the water waves generated are about two times higher than those obtained with a lower $Re_s$ (Figure 20).

The following main results are obtained with the Navier-Stokes model (Figure 21):

- As for the depth-averaged model, the wave amplitude increases quasi linearly with the bed slope, except for the submergence $S_{-1}$ for which the relationship is reversed, and the submergence $S_{-0.5}$, for which the amplitude of the first wave reaches an asymptotic value for slopes larger than 45° (Figure 21).
- We see again that with an initial landslide position crossing the water surface or just above, higher generated water waves are generated compared to more distant initial positions.
- Overall, as for the depth-averaged model, the wave amplitude is two times larger with $Re_s \sim 250$ (Figure 20) than with a lower $Re_s$.

Differences of water heights between the two models are presented in Figure 22. In this figure, the two following statements can be made:

- With the higher $Re_s$, the models give different results, whatever the slope angles or the submergence. Overall, the wave amplitudes obtained with the depth-averaged model are smaller than those obtained with the Navier-Stokes model, except for negative initial submergences and large slope angles. As expected, results are similar for the combination corresponding to the submerged benchmark (Section 4.2) represented by the pink circle in Figure 22(A).
- With the lower $Re_s$, the agreement is much better except for the negative submergence as previously and large slopes (above 45°) for which the depth-averaged model gives higher waves.

Figure 23 shows the sensitivity of both models to the Reynolds number for a given submergence and slope. Below $Re_s \sim 20$, both models tend to give similar results, whereas above this value, the depth-averaged model produces smaller water waves. Nevertheless, the difference between the two models does not increase with the Reynolds but rather reaches a constant value.

## 4.4 Sensitivity study on the turbulence

This section presents a sensitivity analysis on the turbulence using a $k-\epsilon$ model, three different slope angles (35, 45 and 60°) and three different submergences ($S_{-1}$, $S_0$ and $S_{+1}$).

Results of simulated waves in laminar and turbulent modes are shown on Figure 24. Turbulence is shown to play a complex role in some cases enhancing the wave field in others reducing it. A careful investigation of the fields evolution during the simulations allows interesting observations.

First, the slide dynamics with and without turbulence modeling is very similar. Most of the time, the additional viscosity within the slide due to turbulence induces a very slight delay and momentum decrease when slide is transferring energy to the free surface. In some cases, this difference does not change the wave

| | Subaerial | Submerged |
|---|---|---|
| Depth-averaged | 6-15 [16-40] | 0.1-1 [200-2000] |
| Navier-Stokes | 12.8-30 [8-20] | 1-10 [20-200] |

Table 1: Summary table of viscosity $\mu$ and Reynolds number $Re_s$ values (in [ ]) that give the best results relatively to the two benchmarks studied.

field. This happens when there is only a delay of the process but not a change in the direction slide is pushing water (Figure 24A for $S_{+1}$).

In others, the difference in the wave amplitude is very large as in Figure 24C for $S_{+1}$. In this case, the turbulent slide shows an increase of about 10% of its front thickness due to the slightly different interaction with water at the penetration instant compared to the laminar case. This difference induces a larger horizontal momentum transfer to water and subsequently larger waves.

The contrary can occur as in the submarine case shown Figure 24B for $S_{-1}$. In this case, the wave is generated immediately and the initial shape has a critical effect. In this particular situation, the laminar case induces more horizontal momentum transfer that the turbulent case.

We also note that when the slide dynamics and especially the ratio between horizontal and vertical momentum transfer is comparable, even though turbulence is present in water with an additional viscosity of about 100 times the molecular value, this does not change significantly the wave field.

# 5 Discussion

## 5.1 Benchmarks

### 5.1.1 General results

Both the depth-averaged and the Navier-Stokes models can reproduce the benchmarks waves using their own sets of parameters with approximately the same accuracy. The viscosity is generally lower in the depth-averaged model than in the Navier-Stokes model, as summarized in Table 1. However, both models share viscosity values in their intervals of validity: between 12 and 15 Pa.s for the subaerial benchmark (higher than Viroulet et al. (2016), 5 Pa.s, but similar to Clous & Abadie (2019), 10 Pa.s) and around 1 Pa.s for the submerged benchmark (higher than Grilli et al. (2017), 0.01 Pa.s, but similar to Clous & Abadie (2019), 1 Pa.s). This difference between both models is likely due both to the nature of the equations formulations in the depth-averaged model and to the boundary condition that leads to higher viscosity values in the Navier-Stokes model.

### 5.1.2 Relative low influence of the slide viscosity on the waves

Similar water surface elevations are calculated for a range of viscosity values (Sections 4.1 and 4.2 and Table 1). The relative low sensitivity to viscosity value is illustrated by the plateau of lower Q-value depictable in

Figures 3, 7, 11 and 16. We note that the waves in the far-field are even less sensitive to the viscosity.

#### 5.1.3 Poor landslide reproduction especially for the Navier-Stokes model

The optimal parameters to get the correct generated first wave generally do not allow to reproduce the exact measured landslide behavior for both benchmarks and with both models. Hence, as already mentioned by Grilli et al. (2017), the accurate modeling of water waves does not depend on details of the landslide deformation. Moreover, although the equations governing the landslide motion in the depth-averaged model do not make possible to reproduce the bulbous shape of the landslide front, the model allows to obtain correct landslide velocity and quantity of materials entering water for the subaerial benchmark (Figure 5). As regards the submerged benchmark, the landslide simulated by the depth-averaged model is a bit faster than the experimental one (Figure 13). By contrast, the Navier-Stokes model produces a bulbous front that progressively develops while traveling down the slope. This bulbous front is due to a vortex generated at the water/slide interface. In this case, the simulated slide is much slower than in the experiment.

#### 5.1.4 Calibration of the viscosity value

In every practical case, the major issue is to determine the viscosity value. For the subaerial case, the approximation of Ionescu et al. (2015) seems to be valid and both models reproduce the experimental results. For the submerged benchmark, the viscosity values considering in this study are around 10 times lower than those for the subaerial benchmark. A simple extrapolation of these results to other cases is however dangerous. Indeed, this approach requires intrinsic landslide parameters ($\mu$(I) parameters, grain density and grain diameter) to which access is conditioned to a field survey. Moreover, the grain size in the submerged benchmark is about four times greater than the one in the subaerial benchmark, so there is more water between the grains in the submerged case. Because of this water, the landslide becomes more fluid and a lower viscosity is required.

### 5.2 Sensitivity study

#### 5.2.1 Overall results

*Energy transfers*

For both models, the generated waves are higher if the initial landslide position is close to the surface and this may be explained by the combination of the slide front height and the landslide velocity. As shown in Figure 25, the deeper the landslide, the smaller the velocity, so the largest velocities are always calculated for subaerial cases. However, for both models, the most suberial cases result in thinner landslide fronts at the free surface since these landslides stretch rapidly along the slope (see Figure 26 for an illustration with a slope angle of 45° and three submergences, $S_{+1}$, $S_0$ and $S_{-1}$) and the duration close to the free surface is also shorter. In consequences, the energy transfer is reduced for these landslides.

*Slope effect*

The landslide velocity in the depth-averaged model increases with the slope angle for both Reynolds, which leads to higher water waves for large slope angles (Figure 25A). The behavior is more complex in the case of the Navier-Stokes model (Figure 25B).

*Slide Reynolds*

Results in Figure 20 and 21 show that wave amplitudes strongly depend on the Reynolds number. For a given submergence and a given slope angle, wave amplitudes are about two times larger with $Re_s \sim 250$ compared to $Re_s \sim 20$. In the case of the depth-averaged model, landslide velocities are about two times larger for $Re_s \sim 250$ (Figure 25A) which results in larger wave amplitudes. In the case of the Navier-Stokes model, the variation of slide velocities with the slope is more complex (Figure 25B) and the slide shape plays a stronger role in energy transfers.

### 5.2.2 Models concordance

*Importance of the first instants*

For a given slope angle, both models produce similar waves with $Re_s \sim 20$ if the landslide initial position is close to the surface or just above (submergences $S_0$ and $S_{+0.5}$). In these cases, there is no clear difference of landslide behavior in the first instants (see for example the results of the subaerial benchmark in Section 4.1), and the energy transfers should be similar. It is also the case for submergences $S_{+1}$ and $S_{-0.5}$ if the slope angle stays below 45°.

*Differences between models*

For both $Re_s$, if the landslide velocities are similar (e.g. subaerial cases for $Re_s \sim 250$ in Figure 25 A), the waves are larger with the Navier-Stokes model because the depth-averaged model landslide is thinner inherently. Moreover, for small slope angles, the landslide in the depth-averaged model is more likely to spread on both sides of its initial position.

For cases where landslide velocities are larger with the depth-averaged model (e.g. submerged cases for slope angles above 40-45° in Figure 25), the waves are larger too. In these cases, the landslide in the Navier-Stokes model is slowed down by the bulbous shape of the landslide front.

Finally, for large slope angles, the depth-averaged model produces higher waves for the highest submergence, although the average landslide velocity is lower than the one calculated by the Navier-Stokes model (Figure 25). Further analysis of the Navier-Stokes simulations shows that this averaged velocity is not representative of the velocity of the landslide front. In these cases, the front is slowed down by the bottom friction which results in lower water wave amplitudes.

### 5.3 Study limitations

The reproduction of the benchmarks could be improved by using more sophisticated landslide rheology (e.g. a granular rheology instead of a viscous fluid) or boundary conditions but beyond the idea of a perfect reproduction, we were looking for fast solutions in order to use both models in tsunami early warning systems. We note that numerous sets of parameters can lead to very similar water waves and landslide behaviors.

We did not address the influence of the shape of the initial landslide in this study. The triangular shape of the landslide is favorable to the generation of large water waves. However, the slide in the first instants violates the shallow water hypothesis. Further studies with different shapes (such as a more stretched rectangle or an ellipsoid) would be required to reinforce our conclusions.

As seen previously, the initial landslides for the submergence $S_{-1}$ were not fully submerged for small slope angles. Due to the benchmarks geometry, we could not define deeper submergences but it would be definitely interesting to study.

All the Navier-Stokes simulations were conducted in laminar mode. The sensitivity study using a $k-\epsilon$ model showed that the role of turbulence is complex, depending on the submergence and the slope.

## 6 Conclusions

The following main conclusions can be drawn from this study:

- Viscous depth-averaged and Navier-Stokes models can reproduce waves generated by granular slides by calibrating the viscosity but generally the slide dynamics is not properly calculated, especially for the Navier-Stokes model.
- Far enough from the generation area, the wave field is less sensitive to the viscosity value.
- The optimal viscosity range is lower in the depth-averaged model, but there is an overlap between the two models ranges which allows to use the same value with comparable results.
- With this triangle initial slide shape, in general the largest waves are generated when the initial slide is close to the free surface. For higher or lower submergences, the waves are smaller.
- In the depth-averaged model, waves increase continuously with the slope and the slide Reynolds number. The Navier-Stokes model behavior is more complex.
- The concordance of the two models is strongly dependent on the initial submergence and the slide Reynolds number. When the latter is around 20 (*i.e.* relatively high viscosity influence on the slide dynamics), both models behave similarly in terms of waves generated for initial slides crossing or above the free surface. When the slide Reynolds increases, the difference between the two models is much more pronounced.

- The influence of the turbulence on the generated waves is the result of a combination of initial submergence and slope angle, and everything is played out in the very first instants.

# 7 Acknowledgements

We thank the two anonymous reviewers for their constructive comments which improved the quality of this work.

# References

Abadie, S., Harris, J., Grilli, S. & Fabre, R. (2012), 'Numerical modeling of tsunami waves generated by the flank collapse of the Cumbre Vieja Volcano (La Palma, Canary Islands): Tsunami source and near field effects', *Jornal of Geophysical Research* **117**(C05030).

Abadie, S., Morichon, D., Grilli, S. & Glockner, S. (2008), 'VOF/Navier-Stokes numerical modeling of surface waves generated by subaerial landslides', *La Houille Blanche* **1**, 21–26.

Abadie, S., Paris, A., Ata, R., Le Roy, S., Arnaud, G., Poupardin, A., Clous, L., Heinrich, P., Harris, J., Pedreros, R. & Krien, Y. (2020), 'La Palma landslide tsunami: calibrated wave source and assessment of impact on French territories', *Natural Hazards and Earth System Sciences* **20**(11), 3019–3038.

Ataie-Ashtiani, B. & Yavari-Ramshe, S. (2011), 'Numerical simulation of wave generated by landslide incidents in dam reservoirs', *Landslides* **8**, 417–432.

Audusse, E., Caldas Steinstraesser, J., Emerald, L., Heinrich, P., Paris, A. & Parisot, M. (2021), 'Comparison of models for the simulation of landslide generated tsunamis', *ESAIM: Proceedings and Surveys* **70**, 14–30.

Biscarini, C. (2010), 'Computational fluid dynamics modelling of landslide generated water waves', *Landslides* **7**, 117–124.

Bolin, H., Yueping, Y., Xiaoting, C., Guangning, L., Sichang, W. & Zhibing, J. (2014), 'Experimental modeling of tsunamis generated by subaerial landslides: two case studies of the Three Gorges Reservoir, China', *Environmental Earth Sciences* **71**, 3813–3825.

Bondevik, S., Løvholt, F., Harbitz, C., Mangerud, J., Dawson, A. & Svendsen, J. (2005), 'The Storegga slide tsunami - comparing field observations with numerical simulations', *Marine and Petroleum Geology* **22**, 195–208.

Borrero, J., Solihuddin, T., Fritz, H., Lynett, P., Prasetya, G., Skanavis, V., Husrin, S., Kushendratno, Kongko, W., Istiyanto, D., Daulat, A., Purbani, D., Salim, H., Hidayat, R., Asvaliantina, V., Usman, M., Kodijat, A., Son, S. & Synolakis, C. (2020), 'Field Survey and Numerical Modelling of the December 22, 2018 Anak Krakatau Tsunami', *Pure and Applied Geophysics* **177**, 2457–2475.

Bosa, S. & Petti, M. (2011), 'Shallow water numerical model of the wave generated by the Vajont landslide', *Environmental Modelling & Software* **26**, 406–418.

Bregoli, F., Pinzón, A., Medina Iglesias, V. & Gómez Cortés, D. (2013), Experimental studies on 3D impulse waves generated by rapid landslides and debris flows, *in* 'International Conference on Vajont-1963-2013. Thoughts and analyses after 50 years since the catastrophic landslide', Vol. 2013, pp. 115–122.

Bullard, G., Mulligan, R. & Take, W. (2019), 'An Enhanced Framework to Quantify the Shape of Impulse Waves Using Asymmetry', *Journal of Geophysical Research: Oceans* **124**, 652–666.

Clous, L. & Abadie, S. (2019), 'Simulation of energy transfers in waves generated by granular slides', *Landslides* **16**(9), 1663–1679.

Davies, D., Wilson, C. & Kramer, S. (2011), 'Fluidity: A fully unstructured anisotropic adaptive mesh computational modeling framework for geodynamics', *Geochemistry Geophysics Geosystems* **12**(Q06001).

Dutykh, D. & Kalisch, H. (2013), 'Boussinesq modeling of surface waves due to underwater landslides', *Nonlinear Processes in Geophysics* **20**, 267–285.

Enet, F. & Grilli, S. (2007), 'Experimental Study of Tsunami Generation by Three-Dimensional Rigid Underwater Landslides', *Journal of Waterway, Port, Coastal, and Ocean Engineering* **133**(6), 442–454.

Evers, F., Hager, W. & Boes, R. (2019), 'Spatial Impulse Wave Generation and Propagation', *Journal of Waterway, Port, Coastal, and Ocean Engineering* **145**(3), 04019011.

Franz, M., Jaboyedoff, M., Locat, J. & Podladchikov, Y. (2015), Testing a landslide-generated tsunami model. The case of the Nicolet landslide (Québec, Canada), *in* 'Conference GEOQuébec 2015', Québec City, QC, Canada.

Fuhrman, D. & Madsen, P. (2009), 'Tsunami generation, propagation and run-up with a high-order Boussinesq model', *Coastal Engineering* **56**, 747–758.

Glimsdal, S., L'Heureux, J.-S., Harbitz, C. & Løvholt, F. (2016), 'The 29th January 2014 submarine landslide at Statland, Norway–landslide dynamics, tsunami generation, and run-up', *Landslides* **13**(6), 1435–1444.

Grilli, S., Shelby, M. & Kimmoun, O. (2017), 'Modeling coastal tsunami hazard from submarine mass failures: effect of slide rheology, experimental validation, and case studies off the US East Coast', *Natural Hazards* **86**, 353–391.

Grilli, S., Tappin, D., Carey, S., Watt, S., Ward, S., Grilli, A., Engwell, S., Zhang, C., Kirby, J., Schambach, L. & Muin, M. (2019), 'Modelling of the tsunami from the December 22, 2018 lateral collapse of Anak Krakatau volcano in the Sunda Straits, Indonesia', *Scientific Reports* **9**(11946).

Gylfadóttir, S., Kim, J., Helgason, J., Brynjólfsson, S., Höskuldsson, Á., Jóhannesson, T., Harbitz, C. & Løvholt, F. (2017), 'The 2014 Lake Askja rockslide-induced tsunami: Optimization of numerical tsunami model using observed data', *Journal of Geophysical Research: Oceans* **122**, 4110–4122.

Haeussler, P., Gulick, S., McCall, N., Walton, M., Reece, R., Larsen, C., Shugar, D., Geertsema, M., Venditti, J. & Labay, K. (2018), 'Submarine deposition of a subaerial landslide in Taan Fiord, Alaska', *Journal of Geophysical Research: Earth Surface* **123**(10), 2443–2463.

Heidarzadeh, M., Ishibe, T., Sandanbata, O., Muhari, A. & Wijanarto, A. (2020), 'Numerical modeling of the subaerial landslide source of the 22 December 2018 Anak Krakatoa volcanic tsunami, Indonesia', *Ocean Engineering* **195**.

Heinrich, P., Boudon, G., Komorowski, J. C., Sparks, R. S. J., Herd, R. & Voight, B. (2001b), 'Numerical simulation of the December 1997 Debris Avalanche in Montserrat, Lesser Antilles', *Geophysical Research Letters* **28**(13), 2529–2532.

Heinrich, P. & Piatanesi, A. (2000), 'Near-field modeling of the July 17, 1998 tsunami in Papua New Guinea', *Geophysical Research Letters* **27**(19), 3037–3040.

Heller, V. & Spinneken, J. (2015), 'On the effect of the water body geometry on landslide-tsunamis: Physical insight from laboratory tests and 2D to 3D wave parameter transformation', *Coastal Engineering* **104**, 113–134.

Honarmand, M., Shanehsazzadeh, A. & Zandi, S. (2020), '3D numerical simulation of tsunami generation and propagation, case study: Makran tsunami generation and penetrating in Chabahar Bay', *Coastal Engineering* **218**, 108109.

Horrillo, J., Grilli, S., Nicolsky, D., Roeber, V. & Zhang, J. (2015), 'Performance Benchmarking Tsunami Models for NTHMP's Inundation Mapping Activities', *Pure and Applied Geophysics* **172**, 869–884.

Horrillo, J., Wood, A., Kim, G.-B. & Parambath, A. (2013), 'A simplified 3-D Navier-Stokes numerical model for landslide-tsunami: Application to the Gulf of Mexico', *Journal of Geophysical Research: Oceans* **118**, 6934–6950.

Huang, B., Yin, Y., Wang, S., Tan, J. & Liu, G. (2017), 'Analysis of the Tangjiaxi landslide-generated waves in the Zhexi Reservoir, china, by a granular flow coupling model', *Natural Hazards and Earth System Sciences* **17**, 657–670.

Hébert, H., Piatanesi, A., Heinrich, P. & Schindelé, F. (2002), 'Numerical modeling of the September 13, 1999 landslide and tsunami on Fatu Hiva Island (French Polynesia)', *Geophysical Research Letters* **29**(10), 10–13.

Ionescu, I., Mangeney, A., Bouchut, F. & Roche, O. (2015), 'Viscoplastic modeling of granular column collapse with pressure-dependent rheology', *Journal of Non-Newtonian Fluid Mechanics* **219**, 1–18.

Kelfoun, K., Giachetti, T. & Labazuy, P. (2010), 'Landslide-generated tsunamis at Réunion Island', *Journal of Geophysical Research* **115**(F04012).

Kim, G.-B., Cheng, W., Sunny, R., Horrillo, J., McFall, B., Mohammed, F., Fritz, H., Beget, J. & Kowalik, Z. (2020), 'Three Dimensional Landslide Generated Tsunamis: Numerical and Physical Model Comparisons', *Landslides* **17**, 1145–1161.

Le Friant, A., Heinrich, P., Deplus, C. & Boudon, G. (2003), 'Numerical simulation of the last flank-collapse event of Montagne Pelée, Martinique, Lesser Antilles', *Geophysical Research Letters* **30**(2).

Lee, C.-H. & Huang, Z. (2021), 'Multi-phase flow simulation of impulsive waves generated by a sub-aerial granular landslide on an erodible slope', *Landslides* **18**, 881–895.

Lee, C.-H., Low, Y. & Chiew, Y.-M. (2016), 'Multi-dimensional rheology-based two-phase model for sediment transport and applications to sheet flow and pipeline scour', *Physics of Fluids* **28**(053305).

Lefebvre, G., Rosenberg, P., Paquette, J. & Lavallée, J. (1991), 'The September 5, 1987, landslide on the La Grande River, James Bay, Quebec, Canada', *Canadian Geotechnical Journal* **28**(2), 263–275.

L'Heureux, J.-S., Glimsdal, S., Longva, O., Hansen, L. & Harbitz, C. (2011), 'The 1888 shoreline landslide and tsunami in Trondheimsfjorden, central Norway', *Marine Geophysical Research* **32**, 313–329.

L'Heureux, J.-S., Longva, O., Steiner, A., Hansen, L., Vardy, M., Vanneste, M., Haflidason, H., Brendryen, J., Kvalstad, T., Forsberf, C., Chand, S. & Kopf, A. (2012), Identification of weak layers and their role for the stability of slopes at Finneidfjord, Northern Norway, *in* Y. Yamada, K. Kawamura, K. Ikehara, Y. Ogawa, R. Urgeles, D. Mosher, J. Chaytor & M. Strasser, eds, 'Submarine Mass Movements and Their Consequences', Springer Netherlands, Dordrecht, pp. 321–330.

Liu, P.-F., Wu, T.-R., Raichlen, F., Synolakis, C. & Borrero, J. (2005), 'Runup and rundown generated by three-dimensional sliding masses', *Journal of Fluid Mechanics* **536**, 107–144.

Løvholt, F., Pedersen, G. & Gisler, G. (2008), 'Oceanic propagation of a potential tsunami from the La Palma Island', *Journal of Geophysical Research: Oceans* **113**(9), 1–21.

Lynett, P., Gately, K., Wilson, R., Montoya, L., Arcas, D., Aytore, B., Bai, Y., Bricker, J., Castro, M., Cheung, K., David, C., Dogan, G., Escalante, C., González-Vida, J., Grilli, S., Heitmann, T., Horrillo, J., Kânoğlu, U., Kian, R., Kirby, J., Li, W., Macías, J., Nicolsky, D., Ortega, S., Pampell-Manis, A., Park, Y., Roeber, V., Sharghivand, N., Shelby, M., Shi, F., Tehranirad, B., Tolkova, E., Thio, H., Velioğlu, D., Yalçiner, A., Yamazaki, Y., Zaytsev, A. & Zhang, Y. (2017), 'Inter-model analysis of tsunami-induced coastal currents', *Ocean Modelling* **114**, 14–32.

Ma, G., Kirby, J. & Shi, F. (2013), 'Numerical simulation of tsunami waves generated by deformable submarine landslides', *Ocean Modelling* **69**, 146–165.

Macías, J., Vázquez, J., Fernández-Salas, L., González-Vida, J., Bárcenas, P., Castro, M., Díaz-del Río, V. & Alonso, B. (2015), 'The Al-Borani submarine landslide and associated tsunami. A modelling approach', *Marine Geology* **361**, 79–95.

Mangeney, A., Heinrich, P., Roche, R., Boudon, G. & Cheminée, J. (2000), 'Modeling of Debris Avalanche and Generated Water Waves: Application to Real and Potential Events in Montserrat', *Physics and Chemistry of the Earth, Part A: Solid Earth and Geodesy* **25**(9–11), 741–745.

Mazzanti, P. & Vittorio de Blasio, F. (2011), 'The dynamics of coastal landslides: insights from laboratory experiments and theoretical analyses', *Bulletin of Engineering Geology and the Environment* **70**, 411–422.

McFall, B. & Fritz, H. (2016), 'Physical modelling of tsunamis generated by three-dimensional deformable granular landslides on planar and conical island slopes', *Proceedings of the Royal Society A* **472**(20160052).

Mohammed, F. & Fritz, H. (2012), 'Physical modeling of tsunamis generated by three-dimensional deformable granular landslides', *Journal of Geophysical Research* **117**(C11015).

Mulligan, R. & Take, W. (2017), 'On the transfer of momentum from a granular landslide to a water wave', *Coastal Engineering* pp. 16–22.

Naranjo, J., Arenas, M., Clavero, J. & noz, M. (2009), 'Mass movement-induced tsunamis: main effects during the Patagonian Fjordland seismic crisis in Aisén (45°25'S), Chile', *Andrean Geology* **36**(1), 137–145.

Paris, A., Heinrich, P., Paris, R. & Abadie, S. (2020), 'The December 22, 2018 Anak Krakatau, Indonesia, landslide and tsunami: preliminary modeling results', *Pure and Applied Geophysics* **177**, 571–590.

Paris, A., Okal, E., Guérin, C., Heinrich, P., Schindelé, F. & Hébert, H. (2019), 'Numerical modeling of the June 17, 2017 landslide and tsunami events in Karrat Fjord, west Greenland', *Pure and Applied Geophysics* **176**(7), 3035–3057.

Perlin, M. & Bustamante, M. (2016), 'A robust quantitative comparison criterion of two signals based on the Sobolev norm of their difference', *Journal of Engineering Mathematics* **101**, 115–124.

Poupardin, A., Heinrich, P., Frère, A., Imbert, D., Hébert, H. & Flouzat, M. (2017), 'The 1979 Submarine Landslide-Generated Tsunami in Mururoa, French Polynesia', *Pure and Applied Geophysics* **174**, 3293–3311.

Qin, X., Motley, M., LeVeque, R., Gonzalez, F. & Mueller, K. (2018a), 'A comparison of a two-dimensional depth-averaged flow model and a three-dimensional RANS model for predicting tsunami inundation and fluid forces', *Natural Hazards and Earth System Sciences* **18**, 2489–2506.

Qin, X., Motley, M. & Marafi, N. (2018b), 'Three-dimensional modeling of tsunami forces on coastal communities', *Coastal Engineering* **140**, 43–59.

Rauter, M., Hoße, L., Mulligan, R., Take, W. & Løvholt, F. (2021), 'Numerical simulation of impulse wave generation by idealized landslides with OpenFOAM', *Coastal Engineering* **165**(103815).

Redfield, T., Hermanns, R., Oppikofer, T., Duhart, P., Mella, M., Derch, P., Bascuñán, I., Fernandez, J., Arenas, M., Sepúlveda, S., Rebolledo, S., Loew, S., Yugsi Molina, F., Abächerli, A., Henderson, I., Jaboyedoff, M. & Kveldsvik, V. (2011), Analysis of the 2007 earthquake-induced Punta Cola rockslide and tsunami, Aysén Fjord, Patagonia, Chile (45.3° S, 73.0° W), *in* '5th International Conference on Earthquake Geotechnical Engineering', Vol. 12, Santiago, Chile.

Rodriguez, M., Chamot-Rooke, N., Hébert, H., Fournier, M. & Huchon, P. (2013), 'Owen Ridge deep-water submarine landslides: Implications for tsunami hazard along the Oman coast', *Natural Hazards and Earth System Science* **13**, 417–424.

Romano, A., Lara, J., Barajas, G., Di Paolo, B., Bellotti, G., Di Risio, M., Losada, I. & De Girolamo, P. (2020), 'Tsunamis Generated by Submerged Landslides: Numerical Analysis of the Near-Field Wave Characteristics', *Journal of Geophysical Research: Oceans* **125**(7).

Savage, S. & Hutter, K. (1989), 'The motion of a finite mass of granular material down a rough incline', *Journal of Fluid Mechanics* **199**, 177–215.

Serrano-Pacheco, A., Murillo, J. & García-Navarro, P. (2009), 'A finite volume method for the simulation of the waves generated by landslides', *Journal of Hydrology* **273**, 273–289.

Si, P., Shi, H. & Yu, X. (2018), 'A general numerical model for surface waves generated by granular material intruding into a water body', *Coastal Engineering* **142**, 42–51.

Skvortsov, A. & Bornhold, B. (2007), 'Numerical simulation of the landslide-generated tsunami in Kitimat Arm, British Columbia, Canada, 27 April 1975', *Journal of Geophysical Research* **112**(F02028).

Sogut, D. & Yalçiner, A. (2019), 'Performance Comparison of NAMI DANCE and FLOW-3D® Models in Tsunami Propagation, Inundation and Currents using NTHMP Benchmark Problems', *Pure and Applied Geophysics* **176**(7), 3115–3153.

Sue, L., Nokes, R. & Davidson, M. (2011), 'Tsunami generation by submarine landslides: comparison of physical and numerical models', *Environmental Fluid Mechanics* **11**, 133–165.

Tinti, S., Bortolucci, E. & Armigliato, A. (1999), 'Numerical simulation of the landslide-induced tsunami of 1988 on Vulcano Island, Italy', *Bulletin of Volcanology* **61**, 121–137.

Tinti, S., Pagnoni, G. & Zaniboni, F. (2006), 'The landslides and tsunamis of the 30th of December 2002 in Stromboli analysed through numerical simulations', *Bulletin of Volcanology* **68**, 462–479.

Viroulet, S., Sauret, A., Kimmoun, O. & Kharif, C. (2016), Tsunami waves generated by cliff collapse: comparison between experiments and triphasic simulations, *in* E. Pelinovsky & C. Kharif, eds, 'Extreme Ocean Waves', Springer International Publishing, Cham, pp. 173–190.

Wang, J., Ward, S. & Xiao, L. (2015), 'Numerical simulation of the December 4, 2007 landslide-generated tsunami in Chehalis Lake, Canada', *Geophysical Journal International* **201**, 372–376.

Ward, S. & Day, S. (2011), 'The 1963 Landslide and Flood at Vaiont Reservoir Italy. A tsunami ball simulation', *Italian Journal of Geosciences* **130**, 16–26.

Wu, T.-R., Vuong, T.-H.-N., Lin, C.-W., Wang, C.-Y. & Chu, C.-R. (2020), 'Modeling the Slump-Type Landslide Tsunamis Part I: Developing a Three-Dimensional Bingham-Type Landslide Model', *Applied Sciences* **10**(6501).

Xiao, L., Ward, S. & Wang, J. (2015), 'Tsunami Squares Approach to Landslide-Generated Waves: Application to Gongjiafang Landslide, Three Gorges Reservoir, China', *Pure and Applied Geophysics* **172**(12), 3639–3654.

Yavari-Ramshe, S. & Ataie-Ashtiani, B. (2016), 'Numerical modeling of subaerial and submarine landslide-generated tsunami waves–recent advances and future challenges', *Landslides* **13**, 1325–1368.

Yu, M.-L. & Lee, C.-H. (2019), 'Multi-phase-flow modeling of underwater landslides on an inclined plane and consequently generated waves', *Advances in Water Resources* **133**(103421).